

X-Ray Scattering by Nonspherical Grains. I. Oblate Spheroids

B.T. Draine and Khosrow Allaf-Akbari

Princeton University Observatory, Peyton Hall, Princeton, NJ 08544;
draine@astro.princeton.edu, khosrow@astro.princeton.edu

ABSTRACT

We calculate the scattering of X-rays by interstellar dust, for a dust model that reproduces the observed wavelength-dependent extinction and polarization of starlight. On interstellar sightlines that produce appreciable starlight polarization, we predict that the dust-scattered X-ray halo around point sources will have measurable azimuthal asymmetry due to scattering by partially-aligned nonspherical grains. We calculate the expected halo asymmetry. X-ray halo asymmetry provides a new test of interstellar dust models.

Subject headings: ISM: dust, extinction – scattering – X-rays: ISM – X-rays: general

1. Introduction

Interstellar dust grains scatter X-rays through small angles, as was first pointed out by Overbeck (1965), Slysh (1969), and Hayakawa (1970). Because of this scattering, an image of an X-ray point source includes a “halo” of X-rays that have been scattered by dust grains near the line of sight. First observed by Catura (1983) using the *Einstein* observatory, scattered X-ray halos have since been measured by a number of telescopes, including *Einstein* (e.g., Mauche & Gorenstein 1986), *ROSAT* (e.g., Predehl & Schmitt 1995), *Chandra* (e.g., Smith, Edgar, & Shafer 2002), and *XMM-Newton* (e.g., Costantini, Freyberg, & Predehl 2005).

The observed polarization of starlight (Hall 1949; Hiltner 1949) requires that interstellar grains be both appreciably nonspherical and partially aligned, with starlight propagating through the dusty interstellar medium becoming linearly polarized as the result of preferential attenuation of one of the linear polarization modes (“linear dichroism”). In addition to producing polarization of starlight, aligned dust grains produce polarized thermal emission at wavelengths from the far infrared to the microwave. Observers seeking to measure the polarization of the cosmic microwave background must subtract this polarized “galactic foreground” from observations of the microwave sky. Realistic models of nonspherical interstellar grains are therefore of interest for many reasons.

There continue to be many uncertainties concerning the composition and geometry of interstellar grains (for a recent review, see Draine 2003a), and X-ray absorption and scattering can be used to test grain models. We consider a specific grain model consisting of spherical carbonaceous grains and oblate spheroidal silicate grains, with size distributions and size-dependent degree of alignment adjusted to reproduce the observed wavelength dependence of both interstellar extinction and interstellar polarization.

The scattering “halo” produced by a nonspherical grain will not be azimuthally symmetric, and therefore the population of aligned interstellar grains can be expected to produce asymmetric X-ray scattering halos. Here we develop a method for calculating the differential scattering cross section for X-rays incident on grains with arbitrary geometry, and apply it to calculate X-ray scattering halos for a realistic model of interstellar dust.

We find that the X-ray scattering halo produced by this model of aligned interstellar grains has appreciable and observable asymmetry. We propose statistics $R_\ell^{(I)}$ to measure the asymmetry of observed halos. For two models of partially-aligned interstellar grains, we calculate the expected values of $R_2^{(I)}$ and $R_4^{(I)}$, and discuss their observability. The predicted values of $R_2^{(I)}$ should be measurable on sightlines where there is appreciable polarization of starlight. The ratio $R_4^{(I)}/R_2^{(I)}$ is sensitive to the shape of the scattering grains.

The paper is organized as follows: In §2 we discuss anomalous diffraction theory, as applied to interstellar grains, and our implementation of it. In §3 we discuss averaging over the grain rotation expected for partially-aligned suprathermally-rotating grains. In §4 we introduce statistics $R_\ell^{(I)}$ to quantify azimuthal asymmetries in scattering halos. We obtain a realistic grain model in §5, and in §6 we use this model to predict $R_2^{(I)}$ and $R_4^{(I)}$ for sightlines where the magnetic field direction is uniform and perpendicular to the line-of-sight. We discuss using halo asymmetry measurements as a test of grain models in §7. Our results are summarized in §8.

A reader concerned only with the predicted observability of this phenomenon may choose to proceed directly to §7.

2. X-Ray Scattering by Dust: Anomalous Diffraction Theory

2.1. Defining the Scattering Problem

We consider an incident monochromatic electromagnetic plane wave with time dependence $e^{-i\omega t}$ (not explicitly mentioned in the subsequent formulation) and spatial dependence $\exp(i\mathbf{k} \cdot \mathbf{r})$ which is *fully coherent* over the grain volume and *totally non-coherent* over the length-scales of the distances between them. The grain is assumed to consist of material characterized by complex refractive index m . We neglect effects arising from the crystalline or amorphous atomic structure of the grain (Bragg diffraction, for example, affects the scattering only at large angles, where the scattering halo is impossible to observe).

An electromagnetic wave, in a homogeneous (and nonmagnetic) medium, would propagate as

$$\nabla^2 \mathbf{E}(\mathbf{r}, \omega) + k^2 m^2 \mathbf{E}(\mathbf{r}, \omega) = 0 \quad . \quad (1)$$

As usual, the properties of the vector field can be understood by studying the behavior of each of its components, hence reducing our analysis to a scalar theory of scattering, governed by a scalar wave equation $\nabla^2 U(\mathbf{r}, \omega) + k^2 m^2 U(\mathbf{r}, \omega) = 0$. The difficulties arise from the coupling of the different vector components by the boundary conditions at interfaces between different media.

The scattering problem hence reduces to finding how the scatterer responds to an incoming wave U_{inc} , producing an outgoing wave U_{sca} , where $U = U_{\text{inc}} + U_{\text{sca}}$ should satisfy the wave equations above, as well as appropriate boundary conditions. For spheres, an exact series solution, first described by Mie (1908) and Debye (1909) and commonly referred to as “Mie theory”, can be employed provided the sphere is not too large relative to the wavelength of the incident radiation. However, nonspherical targets require other methods.

2.2. Anomalous Diffraction Theory

At X-ray energies materials have refractive indices very close to unity ($|m - 1| \ll 1$) and the dust grains responsible for most of the scattering are usually much larger than the wavelength of the incoming radiation ($ka \gg 1$). In this regime, the scattering and absorption of X-rays can be calculated using an approximation first developed by van de Hulst (1957) and known as “anomalous diffraction theory”, hereafter ADT.

ADT is a combination of ray-tracing optics (applicable because $ka \gg 1$) and Huygens’ principle of *propagation of a scalar field*, applied to cases where the EM wave can enter and propagate through the grain with essentially no reflection or refraction ($|m - 1| \ll 1$).

Consider an incident plane wave $U_{\text{inc}} = U_0 e^{ikz}$, propagating in the $\hat{\mathbf{z}}$ direction. Under the conditions above, the plane wave, once reaching a plane \mathbf{V} located just beyond the grain and normal to the direction of the propagation of the incident wave, will have changed by a fractional amount which we refer to as the *shadow function*, $f(x, y)$:

$$f(x, y) \equiv 1 - \exp[i\Phi(x, y)] \quad , \quad (2)$$

where the complex phase function Φ is

$$\Phi(x, y) \equiv k \int [m(x, y, z) - 1] dz \quad , \quad (3)$$

where $m(x, y, z)$ is the refractive index at the point (x, y, z) .

Once the shadow function is known, Huygens’ principle allows the amplitude of the scattered part of the wave, in the radiation zone, to be calculated as a Fourier transform of the shadow

function over the plane \mathbf{V} :

$$U_{\text{sca}}(r\hat{\mathbf{n}}) = U_0 \frac{\exp(ikr)}{kr} S(\hat{\mathbf{n}}) \quad , \quad (4)$$

$$S(\hat{\mathbf{n}}) = S(k_x, k_y) = \frac{k^2}{2\pi} \int \exp[i(k_x x + k_y y)] f(x, y) dx dy \quad , \quad (5)$$

$$k_x = k(\hat{\mathbf{n}} \cdot \hat{\mathbf{x}}) \quad , \quad (6)$$

$$k_y = k(\hat{\mathbf{n}} \cdot \hat{\mathbf{y}}) \quad . \quad (7)$$

The scattering properties of the grain can be obtained from $S(\hat{\mathbf{n}})$, with the differential scattering cross section given by:

$$\frac{d\sigma_{\text{sca}}}{d\Omega}(\hat{\mathbf{n}}) = \frac{|S(\hat{\mathbf{n}})|^2}{k^2} \quad , \quad (8)$$

The extinction cross section can be obtained from the optical theorem [see, e.g., Bohren & Huffman (1983)]

$$\sigma_{\text{ext}} = \frac{4\pi}{k^2} \text{Re}[S(\hat{\mathbf{z}})] \quad (9)$$

$$= 2 \int (1 - e^{-\Phi_2} \cos \Phi_1) dx dy \quad (10)$$

where $\Phi_1 \equiv \text{Re}(\Phi)$, $\Phi_2 \equiv \text{Im}(\Phi)$. Radiation traversing the grain at (x, y) is attenuated by a factor $e^{-2\Phi_2}$, so that a fraction $(1 - e^{-2\Phi_2})$ of the incident power/area at (x, y) is absorbed by the grain. Thus the absorption cross section in the geometric optics approximation assuming $|m - 1| \ll 1$ (reflection and refraction at interfaces is small) is

$$\sigma_{\text{abs}} = \int (1 - e^{-2\Phi_2}) dx dy \quad , \quad (11)$$

and the total scattering cross section $\sigma_{\text{sca}} = \sigma_{\text{ext}} - \sigma_{\text{abs}}$ is

$$\sigma_{\text{sca}} = \int [1 - 2 \cos \Phi_1 e^{-\Phi_2} + e^{-2\Phi_2}] dx dy \quad (12)$$

$$= \int |f|^2 dx dy \quad . \quad (13)$$

The dimensionless efficiency factors for absorption, scattering, and extinction are here defined to be $Q_{\text{abs}} \equiv \sigma_{\text{abs}}/\pi a_{\text{eff}}^2$, $Q_{\text{sca}} \equiv \sigma_{\text{sca}}/\pi a_{\text{eff}}^2$, $Q_{\text{ext}} \equiv Q_{\text{abs}} + Q_{\text{sca}} = \sigma_{\text{ext}}/\pi a_{\text{eff}}^2$, where for a grain of solid volume V , the effective radius $a_{\text{eff}} \equiv (3V/4\pi)^{1/3}$ is the radius of an equal-volume sphere.

2.3. ADT for a Sphere

For a sphere and scattering angle Θ , the simple form of the shadow function allows $S(\Theta)$ to be written (van de Hulst 1957)

$$S(\Theta) = (ka)^2 \int_0^{\pi/2} du (1 - e^{-i\rho \sin u}) J_0(ka\Theta \cos u) \sin u \cos u \quad , \quad (14)$$

$$\rho \equiv 2ka(m-1) \quad , \quad (15)$$

where J_0 is the Bessel function of order 0. The extinction, absorption, and scattering efficiency factors are

$$Q_{\text{ext}} = 2 + \frac{4 \{ \cos 2\beta - e^{-\rho_2} [\cos(\rho_1 - 2\beta) - |\rho| \sin(\rho_1 - \beta)] \}}{|\rho|^2} \quad (16)$$

$$Q_{\text{abs}} = 1 + \frac{e^{-2\rho_2}}{\rho_2} + \frac{e^{-2\rho_2} - 1}{2\rho_2^2} \quad (17)$$

$$Q_{\text{sca}} = Q_{\text{ext}} - Q_{\text{abs}} \quad (18)$$

where $\rho_1 \equiv \text{Re}(\rho)$, $\rho_2 \equiv \text{Im}(\rho)$, and $\beta \equiv \arctan(\rho_2/\rho_1)$.

2.4. The DADT code

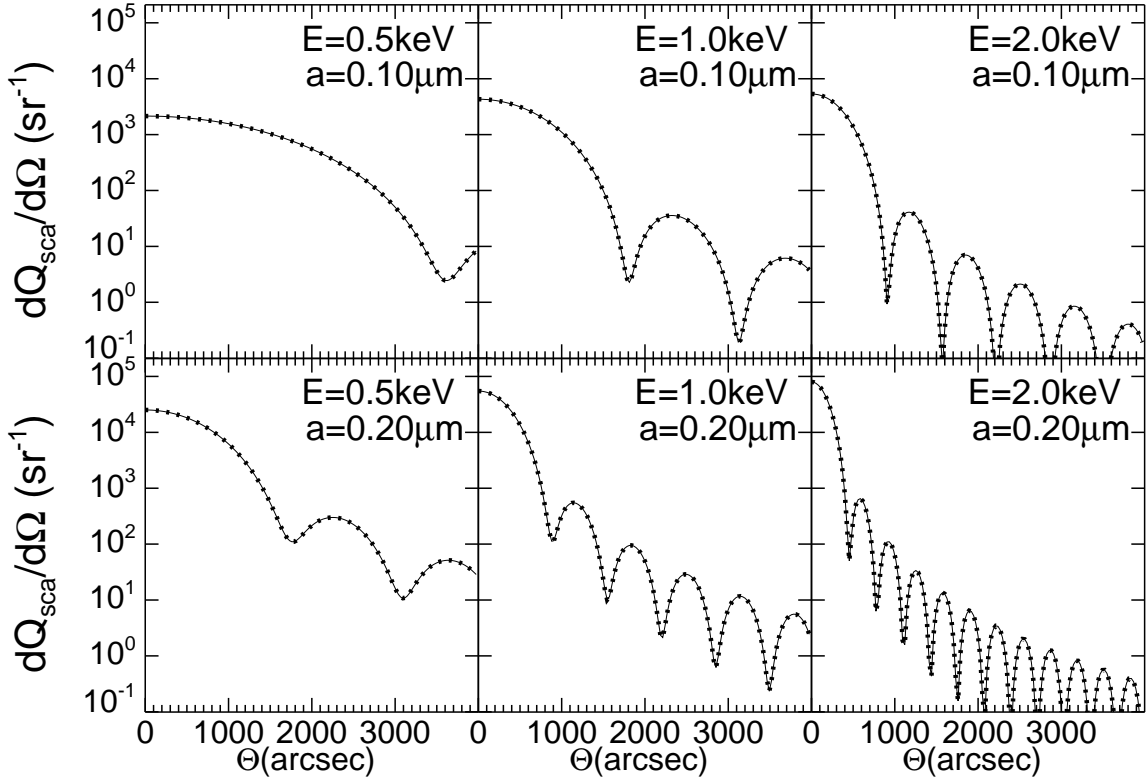


Fig. 1.— Differential scattering cross section for MgFeSiO_4 silicate spheres with radii $a = 0.1$ and $0.2 \mu\text{m}$ at $E = 0.5, 1$ and 2 keV calculated with Mie theory (solid curve) and DADT (dots). The two methods coincide to within the accuracy of the plot. The refractive index at $E = 0.5, 1$ and 2 keV is taken to be $m = 1 - 2.079 \times 10^{-3} + 3.201 \times 10^{-3}i$, $1 - 7.152 \times 10^{-4} + 1.887 \times 10^{-4}i$, and $1 - 1.920 \times 10^{-4} + 2.807 \times 10^{-5}i$, respectively (Draine 2003b).

For general shapes, eq. (5) requires finding $f(x, y)$ numerically, followed by a two dimensional integration for each scattering direction $\hat{\mathbf{n}}$. Because we will typically be interested in many scattering directions, it is advantageous to employ fast Fourier transform (FFT) methods to find $S(\hat{\mathbf{n}})$.

Our ADT-code, hereafter referred to as **Discrete-ADT** code, DADT for short, samples the shadow function on a (x, y) -grid of $2^{11} \times 2^{11}$ points, with $\sim 2^7 \times 2^7$ points within the projected area of the grain.¹ A 2-dimensional FFT then yields $S(k_x, k_y)$ over a rectangular (k_x, k_y) grid of $2^{11} \times 2^{11}$ points. The single-precision FFT code **GPFA**, developed by Temperton (1983, 1992) is employed for the 2-D FFT. The resulting $S(k_x, k_y)$ is then transformed onto a $2^{11} \times 2^{11}$ polar lattice (equal number of divisions in ϕ and Θ) using a two-dimensional cubic spline.

We have tested DADT by comparing the scattering halo pattern calculated using DADT to results calculated with the Mie theory implementation **MIEVO** by Wiscombe (1980, 1996), after conversion to double precision arithmetic. Figure 1 shows the differential scattering cross section calculated for $a = 0.1$ and $0.2\mu\text{m}$ silicate spheres at $E = 0.5, 1,$ and 2keV . The results calculated with DADT and those calculated with **MIEVO** are indistinguishable. Because **MIEVO** and DADT follow entirely different approaches to the calculation, this confirms the accuracy of both for the cases considered. Note that absorption is strong in some of the cases shown: $\text{Im}(m)ka = 1.62$ for $a = 0.2\mu\text{m}$ and $E = 0.5\text{keV}$. ADT requires $|m - 1| \ll 1$, but $\text{Im}(m)ka$ need not be small. The validity condition $|m - 1| \lesssim 0.01$ is fulfilled for silicates for $E > 250\text{eV}$. The ray optics validity condition $ka \gtrsim 10^2$ is satisfied for $a > 0.08\mu\text{m}(250\text{eV}/E)$.

2.5. Results

Having verified that DADT yields accurate results for X-ray scattering by spheres, we now apply it to calculate X-ray scattering by oblate spheroids. Figure 2 shows the differential scattering cross section for axial ratio $b/a = \sqrt{2}$ oblate silicate spheroids with symmetry axis perpendicular to the line-of-sight for two sizes ($a_{\text{eff}} = 0.1$ and $0.2\mu\text{m}$) and three energies ($E = 0.5, 1, 2\text{keV}$). The differential scattering cross section $d\sigma/d\Omega(\Theta, \phi)$ is shown as a function of Θ for $\phi = 0$ (the direction of the short axis of the grain) and $\phi = 90^\circ$. It is apparent that the scattering is more extended in the $\phi = 0$ direction: it is easily shown that for this orientation of an oblate spheroid, the halo extent in the $\phi = 0$ direction is larger than the extent in the $\phi = 90^\circ$ direction by exactly the factor b/a .

Figure 2 also shows that as a_{eff} or E are increased, the angular extent of the halo shrinks, scaling as $1/(a_{\text{eff}}E)$.

¹The shadow function $f(x, y)$ is nonzero only over the projection of the target onto the (x, y) -plane. However, any discrete Fourier transform requires that the range of integration be extended to distances $r \gg a$ to evaluate $S(\hat{\mathbf{n}})$ for angles within the first minimum of the scattering halo. These angles play a crucial role in our understanding of the halo properties, and we therefore extend our grid by a factor 2^4 in each direction, providing an angular resolution of $\sim 1/10$ the angle of the first minimum of $S(\hat{\mathbf{n}})$.

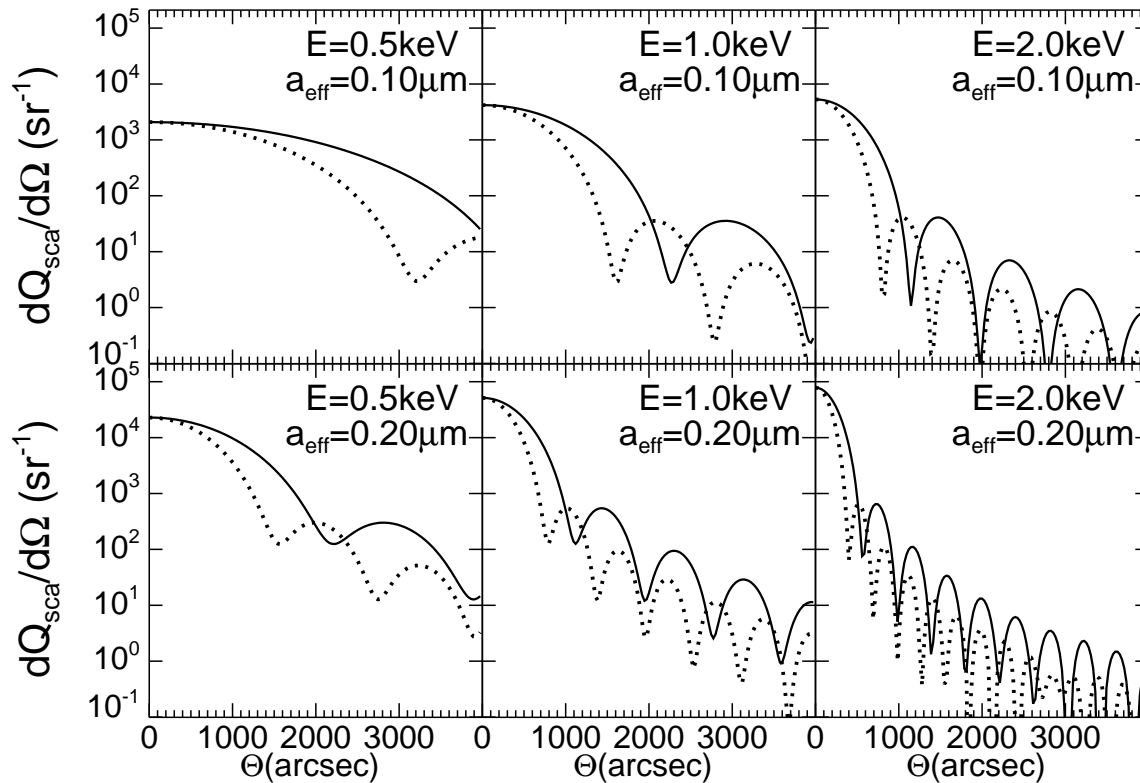


Fig. 2.— Differential scattering cross section for $b/a = \sqrt{2}$ oblate silicate spheroid with its symmetry-axis perpendicular to the line of sight and in the direction $\phi = 0$, for $a_{\text{eff}} = 0.1\mu\text{m}$ and $0.2\mu\text{m}$. Results are shown for $\phi = 0^\circ$ (solid line) and $\phi = 90^\circ$ (dotted line). Scattering is more extended in the direction parallel to the “short axis” of the shadow function.

Figure 3 shows the scattering for the same two grains as in Figure 2, but now with the grains oriented with symmetry axis parallel to the line-of-sight. For this orientation the scattering is azimuthally symmetric. The angular extent (e.g., locations of minima and maxima) is similar to the scattering in the $\phi = 90^\circ$ direction in Fig. 2, being proportional to $1/b$ in both cases.

Figure 4 shows contours of constant $d\sigma/d\Omega$ for oblate spheroids, with symmetry axis (short axis) in the \hat{x} direction. The contours are ellipses with axial ratios b/a .

3. Scattering by Spinning, Precessing Grains

In this section we give a few general results concerning symmetries in scattering by populations of spinning grains precessing around the local magnetic field. Rotation and precession are assumed to be rapid enough to ensure phase averaging over rotation angle and precession angle.

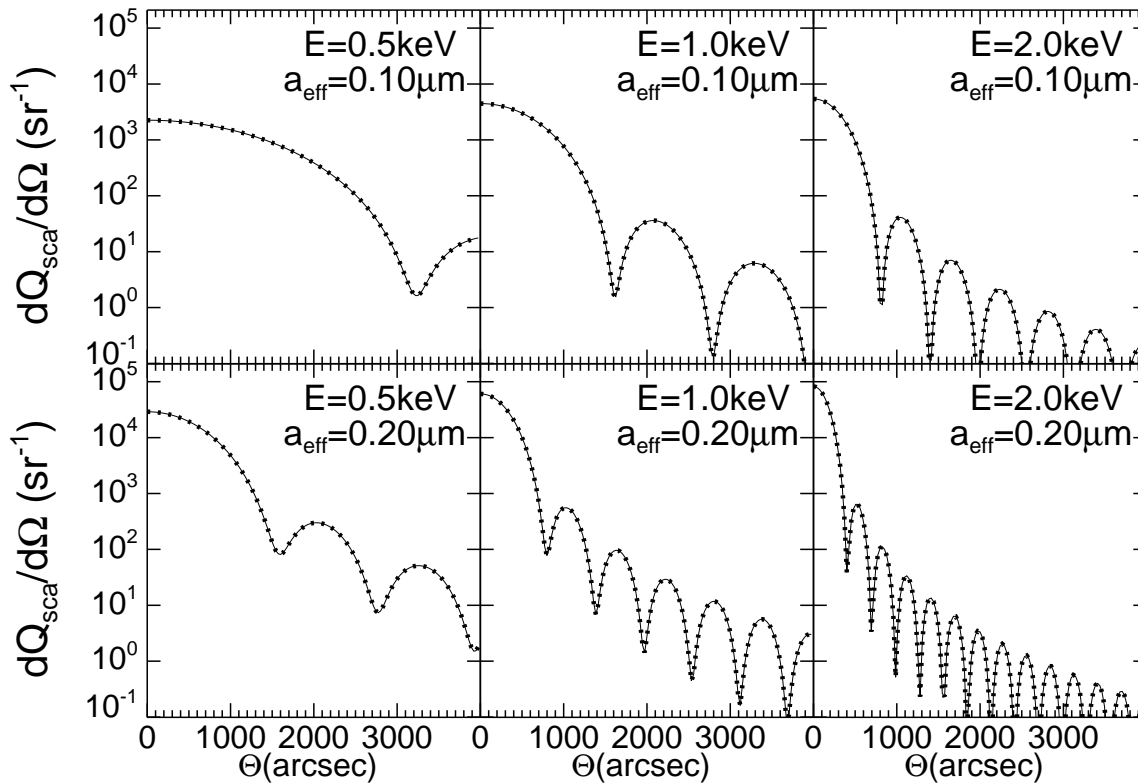


Fig. 3.— Same as Fig. 2, but for the grain symmetry axis parallel to the line of sight. Results are shown for $\phi = 0^\circ$ (solid line) and $\phi = 90^\circ$ (dotted line); the two curves coincide because of symmetry.

Consider radiation propagating in the \hat{z} direction. Suppose that there is a magnetic field \mathbf{B} in the $\hat{x} - \hat{z}$ plane; let $\Theta_{\mathbf{Bz}}$ be the angle between \mathbf{B} and \hat{z} . The scattering direction is defined by scattering angles (Θ, ϕ) , where Θ is the deflection angle, and ϕ is an azimuthal angle with $\phi = 0$ corresponding to scattering in the $\hat{x} - \hat{z}$ plane.

Scattering by a sphere, or by a grain that is rotationally symmetric about the line of sight, will be azimuthally symmetric. This will also be the case for scattering by a population of arbitrarily-shaped grains if the distribution function for grain orientations is azimuthally symmetric about the line of sight.

Nonspherical grains that are not randomly oriented will produce scattering that will not be azimuthally symmetric. Grains will in general be spinning rapidly; let \mathbf{J} be the instantaneous direction of the grain angular momentum. The torques acting on a spinning grain have been discussed elsewhere (e.g., Draine & Weingartner 1997). The spinning grain will acquire a magnetic moment $\mu \parallel -\mathbf{J}$ due to the Barnett effect. The $\mu \times \mathbf{B}$ torque drives precession of \mathbf{J} around \mathbf{B} . The precession period is short, of order weeks, so that we may assume a uniform distribution of \mathbf{J} around the precession cone. The distribution of directions $\hat{\mathbf{J}}$ will therefore be determined by $\Theta_{\mathbf{Bz}}$

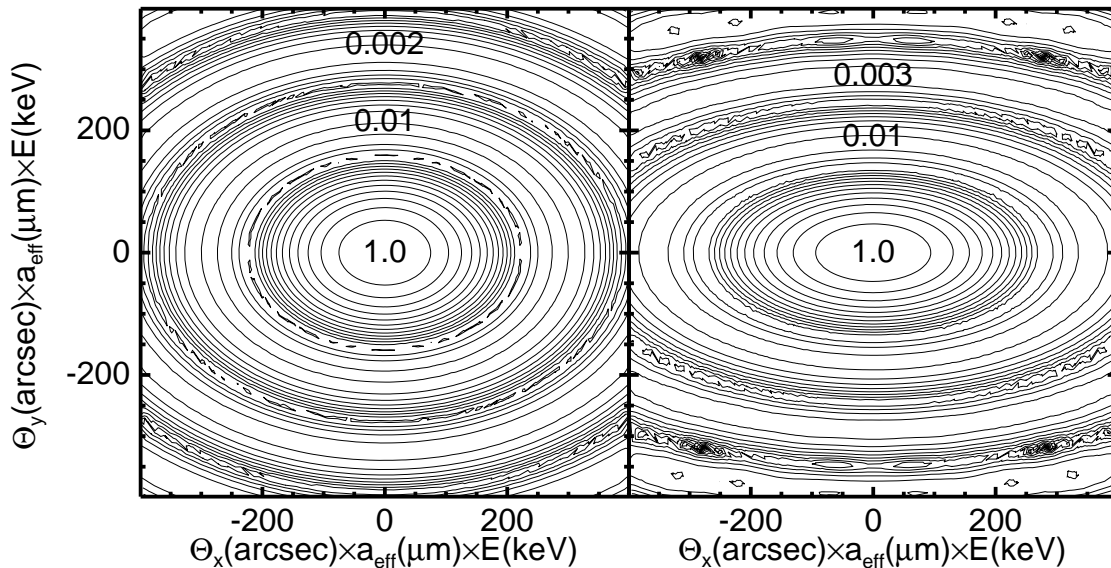


Fig. 4.— Contours of constant $[d\sigma/d\Omega(\Theta, \phi)]/[d\sigma/d\Omega(0, 0)] = 10^{-n/5}$ for grains with $b/a = \sqrt{2}$ (left panel) and $b/a = 2$ (right panel), with short axis in the \hat{x} direction. Contours at local maxima are labelled; regions where the contours are closely-spaced are minima. The contours should ideally be perfect ellipses; deviations result from the discreteness of our grid and inaccuracies of interpolations by the contour-plotting software. Results were calculated for $a_{\text{eff}} = 0.2\mu\text{m}$ silicate grains and $E = 1\text{keV}$, but the plots apply to other values of a_{eff} , E , and composition provided the ADT validity criteria $|m - 1| \ll 1$ and $ka \gg 1$ are satisfied and, in addition, $|m - 1|ka \ll 1$.

and the angle $\Theta_{\mathbf{BJ}}$ between \mathbf{B} and \mathbf{J} .

We will assume the aligned grains in the present study to be spinning suprathermally, i.e., with rotational kinetic energy $E_{\text{rot}} \gg kT_{\text{gr}}$, where T_{gr} is the grain temperature. For a suprathermally-rotating grain with fixed angular momentum \mathbf{J} , dissipation resulting from viscoelasticity, the Barnett effect, or nuclear magnetism (Purcell 1979; Lazarian & Draine 1999a,b) will cause the grain to minimize its rotational kinetic energy, and therefore to be oriented with $\hat{\mathbf{a}}_1 \parallel \mathbf{J}$ or $\hat{\mathbf{a}}_1 \parallel -\mathbf{J}$, where $\hat{\mathbf{a}}_1$ is the principal axis of largest moment of inertia. The states with $\hat{\mathbf{a}}_1 \parallel \mathbf{J}$ and $\hat{\mathbf{a}}_1 \parallel -\mathbf{J}$ have the same energy, and we will assume them to be equally occupied. Therefore, for a suprathermally rotating grain, the distribution of $\hat{\mathbf{a}}_1$ in space will be fully determined by $\Theta_{\mathbf{Bz}}$ and the alignment angle $\Theta_{\mathbf{BJ}}$.

It is convenient to define a normalized scattering function

$$\bar{\sigma}(\Theta_s, \phi_s) \equiv \frac{1}{\sigma_{\text{sca}}} \left\langle \frac{d\sigma_{\text{sca}}}{d\Omega} \right\rangle \quad (19)$$

$$\sigma_{\text{sca}} \equiv \int d\Omega \left\langle \frac{d\sigma_{\text{sca}}}{d\Omega} \right\rangle, \quad (20)$$

where (Θ_s, ϕ_s) are scattering angles, $\langle d\sigma_{\text{sca}}/d\Omega \rangle$ is the differential scattering cross section per H nucleon summed over the different grain types and averaged over the ensemble of grain orientations,

and σ_{sca} is the total scattering cross section per H nucleon. With this definition, $\int \tilde{\sigma} d\Omega = 1$. For suprathermally-rotating grains, the normalized scattering function $\tilde{\sigma}(\Theta, \phi)$ is determined by the grain properties (composition, size, and geometry), the angle $\Theta_{\mathbf{Bz}}$ and the distribution function for the alignment angle $\Theta_{\mathbf{BJ}}$ for each grain type.

The function $\tilde{\sigma}$ will satisfy the symmetry²

$$\tilde{\sigma}(\Theta, \phi) = \tilde{\sigma}(\Theta, -\phi) \quad (21)$$

and can therefore be written

$$\tilde{\sigma}(\Theta, \phi) = a_0(\Theta) + 2 \sum_{\ell=1}^{\infty} a_{\ell}(\Theta) \cos(\ell\phi) \quad , \quad (22)$$

$$a_{\ell}(\Theta) \equiv \frac{1}{2\pi} \int_0^{2\pi} d\phi \tilde{\sigma}(\Theta, \phi) \cos(\ell\phi) \quad . \quad (23)$$

If $\Theta_{\mathbf{Bz}} = 0$ or $\pi/2$, the scattering will be symmetric upon reflection through the \mathbf{y} axis:

$$\tilde{\sigma}(\Theta, \phi) = \tilde{\sigma}(\Theta, \pi - \phi) \quad , \quad (24)$$

$$a_{\ell} = 0 \quad \text{for odd } \ell. \quad (25)$$

For $0 < \Theta_{\mathbf{Bz}} < \pi/2$, the symmetry (24) is not strictly required for scattering by dust. However, when anomalous diffraction theory applies, the symmetry condition (24) will also apply,³ in which case $\tilde{\sigma}(\Theta, \phi)$ can be written

$$\tilde{\sigma}(\Theta, \phi) = a_0(\Theta) + 2 \sum_{\ell=1}^{\infty} a_{2\ell}(\Theta) \cos(2\ell\phi) \quad . \quad (26)$$

4. Azimuthal Asymmetry in X-Ray Scattering by a Nonspherical Grain

4.1. Asymmetry of Grain Scattering

Consider some specific magnetic field direction $\Theta_{\mathbf{Bz}}$, and an ensemble of grains with some specified distribution function for the alignment angle $\Theta_{\mathbf{BJ}}$. The function

$$g^{(\sigma)}(\Theta_1, \Theta_2) \equiv \int_{\Theta_1}^{\Theta_2} d\Theta \sin \Theta \int_0^{2\pi} d\phi \tilde{\sigma}(\Theta, \phi) \quad (27)$$

²Eq. (21) need not be satisfied for arbitrary grains, but will be satisfied if every grain in the population has a mirror-image counterpart.

³This is a consequence of the scattering depending only on the shadow function (2). For any \mathbf{J} , rotation of the grain around \mathbf{J} and equal numbers of grains with $\hat{\mathbf{a}}_1 \parallel \mathbf{J}$ and $\hat{\mathbf{a}}_1 \parallel -\mathbf{J}$ together ensure that the ensemble of shadow functions is symmetric under reflection $x \rightarrow -x$, in which case $\tilde{\sigma}(\Theta, \phi) = \tilde{\sigma}(\Theta, \pi - \phi)$.

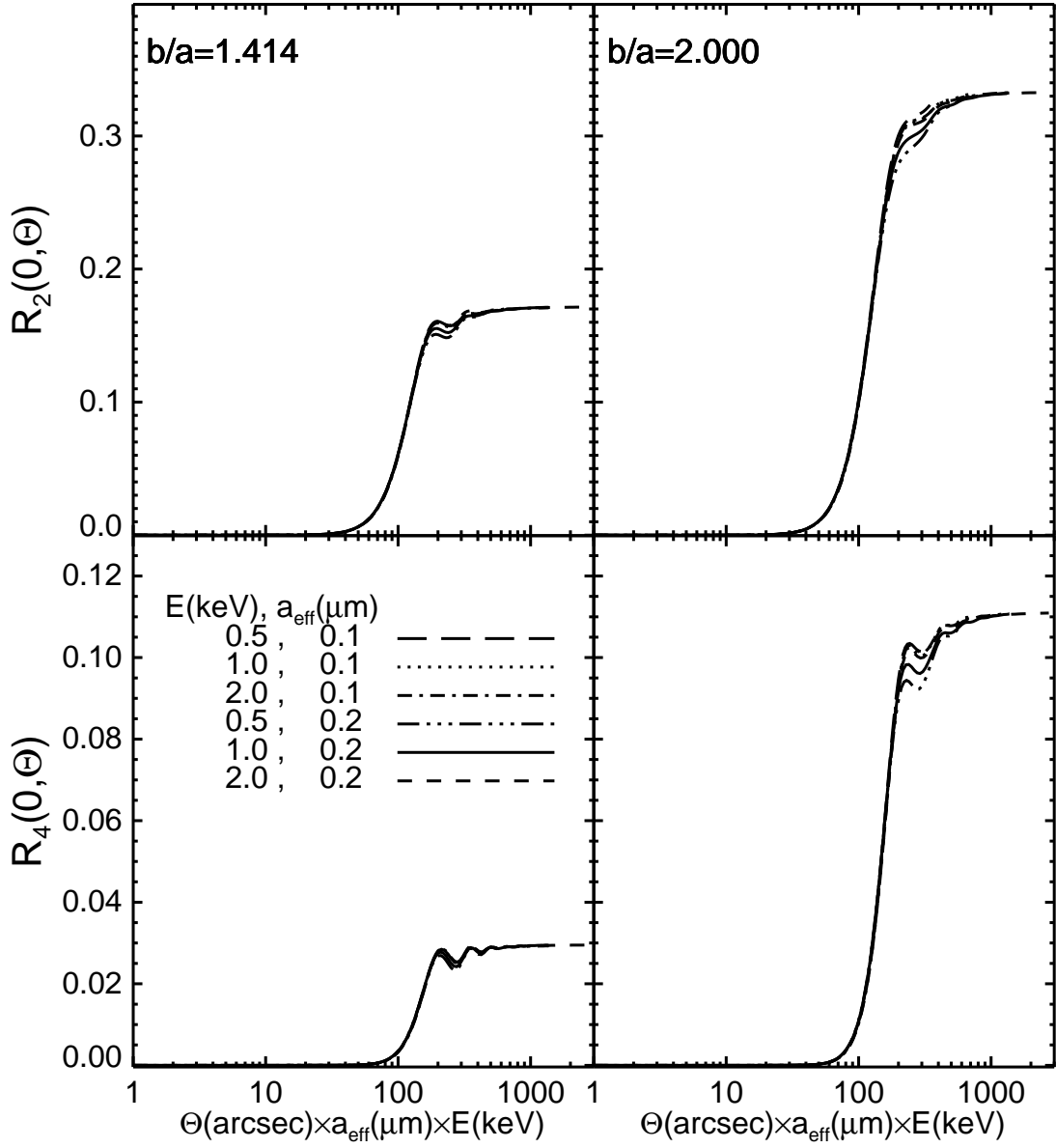
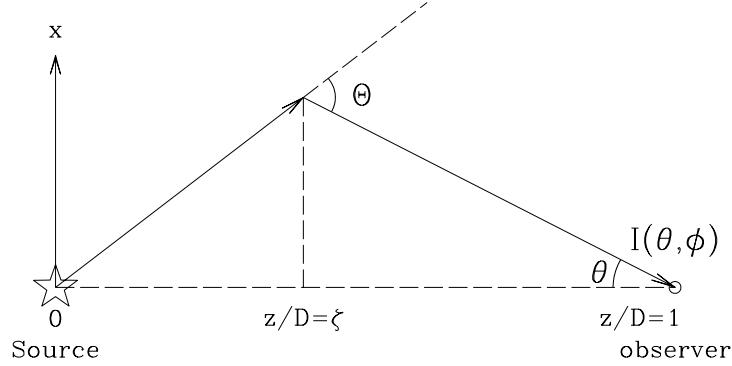


Fig. 5.— $R_2^{(\sigma)}(0, \Theta)$ and $R_4^{(\sigma)}(0, \Theta)$ vs. $\Theta a_{\text{eff}} E$ for $b/a = \sqrt{2}$ and $b/a = 2$ silicate spheroids. Results are shown for $a_{\text{eff}} = 0.1$ and $0.2 \mu\text{m}$, and for $E = 0.5, 1, 2$ keV.

$$= 2\pi \int_{\Theta_1}^{\Theta_2} d\Theta \sin \Theta a_0(\Theta) \quad (28)$$

gives the fraction of the scattering that is within the annulus $[\Theta_1, \Theta_2]$.

For scattering angles in the annulus $[\Theta_1, \Theta_2]$ the degree of azimuthal asymmetry of the differ-



B. T. Draine 2006.07.08.

Fig. 6.— Geometry for scattering of X-rays by a dust grain. Angles are exaggerated; actual halo angles θ are $\lesssim 1^\circ$.

ential scattering cross section can be characterized by functions

$$R_\ell^{(\sigma)}(\Theta_1, \Theta_2) \equiv \frac{\int_{\Theta_1}^{\Theta_2} d\Theta \sin \Theta \int_0^{2\pi} d\phi \cos(\ell\phi) \tilde{\sigma}(\Theta, \phi)}{\int_{\Theta_1}^{\Theta_2} d\Theta \sin \Theta \int_0^{2\pi} d\phi \tilde{\sigma}(\Theta, \phi)} \quad (29)$$

$$= \frac{\int_{\Theta_1}^{\Theta_2} d\Theta \sin \Theta a_\ell(\Theta)}{\int_{\Theta_1}^{\Theta_2} d\Theta \sin \Theta a_0(\Theta)} \quad \text{for } \ell \geq 1 \quad . \quad (30)$$

The symmetry condition (24) yields $R_\ell^{(\sigma)} = 0$ for odd ℓ .

We will be interested primarily in the quadrupolar asymmetry, characterized by the function $R_2^{(\sigma)}$. Figure 5 shows $R_2^{(\sigma)}(0, \Theta)$ for perfectly aligned oblate spheroids. $R_2^{(\sigma)}(0, \Theta)$ rises rapidly from zero to a value ~ 0.17 for $b/a = \sqrt{2}$ and ~ 0.33 for $b/a = 2$. We also see that the octupole/quadrupole ratio $R_4^{(\sigma)}/R_2^{(\sigma)}$ is sensitive to the grain shape: for $\Theta a_{\text{eff}} E \gtrsim 3.5$ arcmin $\mu\text{m keV}$, the ratio $R_4^{(\sigma)}/R_2^{(\sigma)}$ increases from 0.17 to 0.33 as b/a is increased from $\sqrt{2}$ to 2.

4.2. Asymmetry of X-Ray Scattering Halo

The geometry of X-ray scattering is illustrated in Figure 6; note that X-ray scattering is significant only for small scattering angles Θ , and therefore only for small halo angles θ . If the dust grain distribution in space is $\rho(z)$ (assumed, for the moment, to be independent of x and y for small displacements from the line-of-sight), then, for a steady isotropic source with luminosity per unit frequency L_ν , the specific intensity of singly-scattered photons is given by (see, e.g., Draine & Tan 2000)

$$I_\nu(\theta, \phi) \approx \frac{L_\nu}{4\pi D^2} e^{-\tau_{\text{ext}}} \frac{1}{\cos \theta} \tau_{\text{sca}} \int_0^1 d\zeta \frac{\tilde{\rho}(\zeta) \tilde{\sigma}(\Theta_s, \phi)}{\zeta^2 + (1 - \zeta)^2 \tan^2 \theta} \quad , \quad (31)$$

$$\tilde{\rho}(\zeta) \equiv \frac{\rho(z = \zeta D)}{D^{-1} \int_0^D \rho(z) dz} \quad , \quad (32)$$

$$\Theta_s(\zeta, \theta) = \theta + \arctan \left[\frac{(1 - \zeta) \tan \theta}{\zeta} \right] \quad , \quad (33)$$

$$\tau_{\text{sca}} \equiv N_{\text{H}} \sigma_{\text{sca}} \quad , \quad (34)$$

provided $\tau_{\text{sca}} \lesssim 0.3$ so that multiple scattering can be neglected. Let $I(\theta, \phi)$ be the observed intensity of scattered X-rays. The function

$$g^{(I)}(\theta_1, \theta_2) \equiv \frac{\int_{\theta_1}^{\theta_2} d\theta \sin \theta \int_0^{2\pi} d\phi I(\theta, \phi)}{\int_0^{\pi/2} d\theta \sin \theta \int_0^{2\pi} d\phi I(\theta, \phi)} \quad , \quad (35)$$

gives the fraction of the total scattered power that falls in the annulus $[\theta_1, \theta_2]$. The azimuthal asymmetry of the scattered halo in the annulus $[\theta_1, \theta_2]$ can be measured by the function

$$R_\ell^{(I)}(\theta_1, \theta_2) \equiv \frac{\int_{\theta_1}^{\theta_2} d\theta \sin \theta \int_0^{2\pi} d\phi \cos(\ell\phi) I(\theta, \phi)}{\int_{\theta_1}^{\theta_2} d\theta \sin \theta \int_0^{2\pi} d\phi I(\theta, \phi)} \quad . \quad (36)$$

For optically-thin scattering by dust aligned by a uniform magnetic field perpendicular to the line-of-sight, we can calculate $R_\ell^{(I)}$:

$$R_\ell^{(I)}(\theta_1, \theta_2) = \frac{\int_{\theta_1}^{\theta_2} d\theta \tan \theta \int_0^1 d\zeta a_\ell(\Theta_s) \tilde{\rho}(\zeta) / [\zeta^2 + (1 - \zeta)^2 \tan^2 \theta]}{\int_{\theta_1}^{\theta_2} d\theta \tan \theta \int_0^1 d\zeta a_0(\Theta_s) \tilde{\rho}(\zeta) / [\zeta^2 + (1 - \zeta)^2 \tan^2 \theta]} \quad , \quad (37)$$

where the a_ℓ are given by eq. (23). If we assume $\rho(\zeta) = 0$ for $\zeta \ll 1$ (i.e., negligible scattering from dust very near the source) we can assume $\tan \theta \ll 1$, $\theta \approx \zeta \Theta_s$, and approximate (37) by

$$R_\ell^{(I)}(\theta_1, \theta_2) \approx \frac{\int_0^1 d\zeta \tilde{\rho}(\zeta) \int_{\theta_1/\zeta}^{\theta_2/\zeta} a_\ell(\theta) \theta d\theta}{\int_0^1 d\zeta \tilde{\rho}(\zeta) \int_{\theta_1/\zeta}^{\theta_2/\zeta} a_0(\theta) \theta d\theta} \quad . \quad (38)$$

5. Models for Aligned Interstellar Grains

5.1. Observed Polarization

Our objective is to calculate X-ray scattering from a realistic model of partially aligned nonspherical dust grains, with the size distribution and degree of alignment constrained to reproduce both extinction and polarization as a function of wavelength.

The observed polarization of starlight (Hall 1949; Hiltner 1949) demonstrates that interstellar grains are both nonspherical and systematically aligned. We take the polarization as a function of

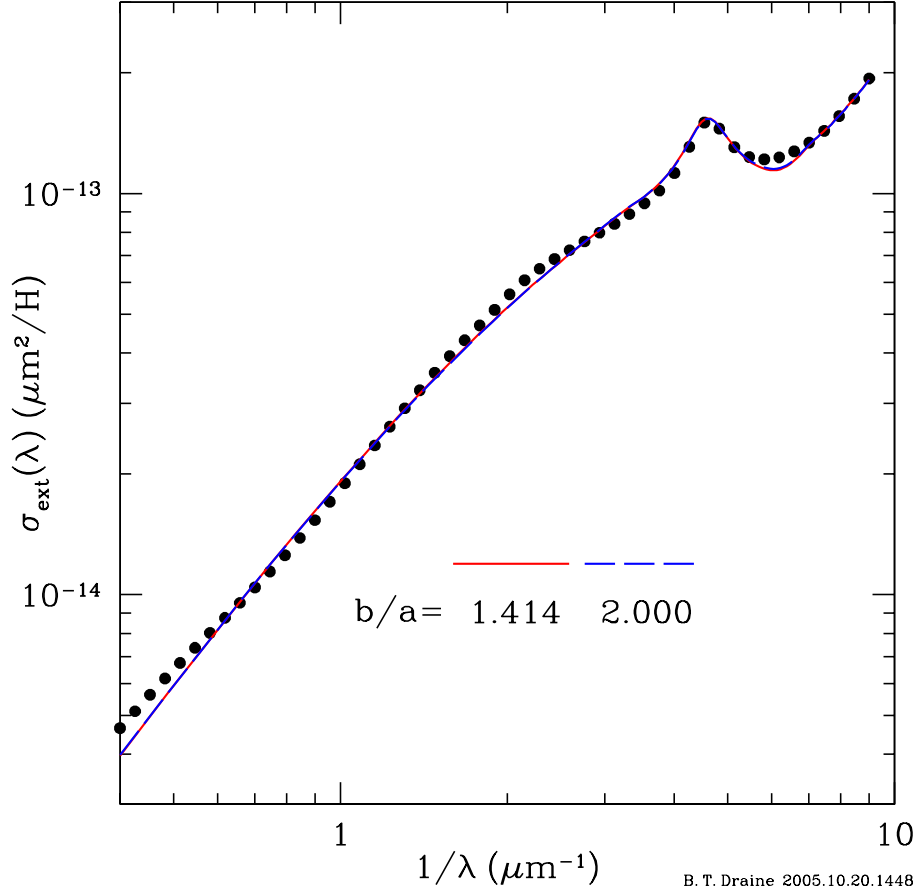


Fig. 7.— Extinction for randomly-oriented grains with the size distribution shown in Figure 9. Dotted curve shows the observed extinction law that was applied as a constraint on the model. The extinction for the models with $b/a = \sqrt{2}$ (solid line) and 2 (broken line) nearly coincide and cannot be distinguished in this plot.

wavelength to be empirically described by the “Serkowski law” (Serkowski 1973) for $\lambda < \lambda_x$, and a power-law for $\lambda_x < \lambda < 5\mu\text{m}$:

$$p(\lambda) \approx p_{\text{max}} \exp \left\{ -K [\ln(\lambda/\lambda_{\text{max}})]^2 \right\} \quad \text{for } \lambda < \lambda_x \quad , \quad (39)$$

$$p(\lambda) \approx p_{\text{max}} \exp(-\beta^2/4K) (\lambda_x/\lambda)^\beta \quad \text{for } \lambda_x < \lambda < 5\mu\text{m} \quad , \quad (40)$$

$$\lambda_x = \lambda_{\text{max}} \exp(\beta/2K) \quad . \quad (41)$$

The wavelength of peak polarization has a typical value $\lambda_{\text{max}} \approx 0.55\mu\text{m}$, but varies from one sightline to another. The value of K is correlated with λ_{max} , with $K \approx 0.91(\lambda_{\text{max}}/0.55\mu\text{m}) + 0.01$ (Whittet et al. 1992). We take $\beta = 1.7$, within the range observed by Martin et al. (1992). For $\lambda_{\text{max}} = 0.55\mu\text{m}$, we have $K = 0.92$, and $\lambda_x = 1.39\mu\text{m}$.

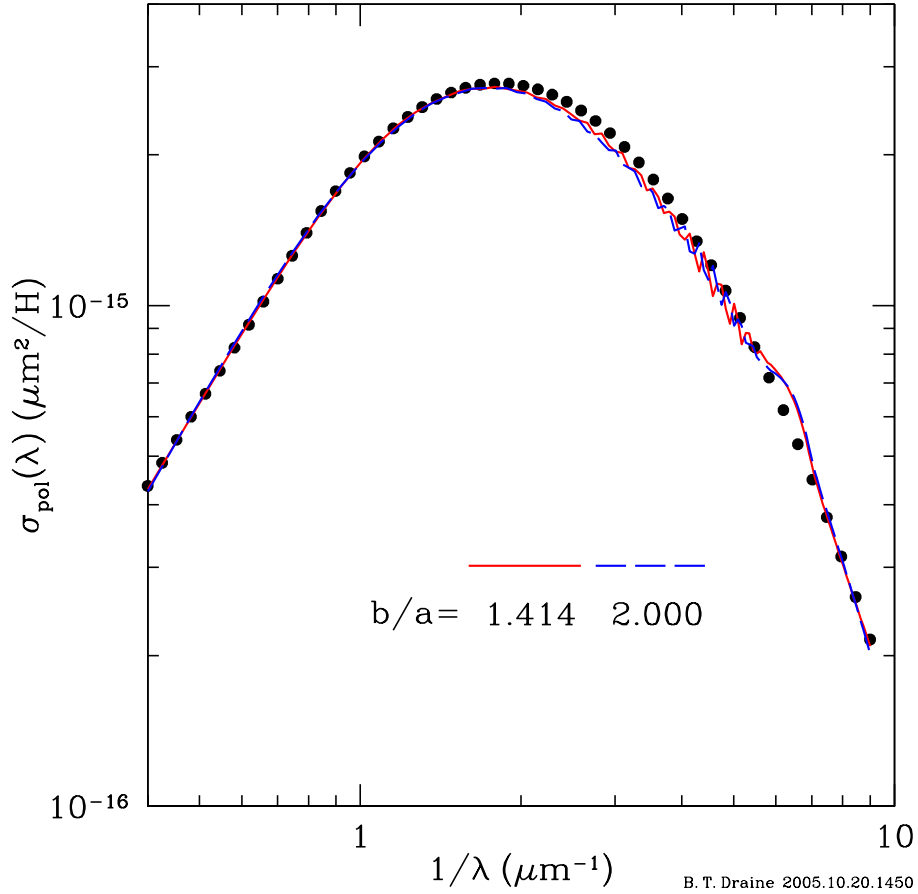


Fig. 8.— Polarization cross section $\sigma_{\text{pol}}(\lambda)$ for a line of sight perpendicular to the local magnetic field, for oblate silicate spheres with the size distribution of Fig. 9 and size-dependent alignment fraction of Fig. 10. Dotted curve is the observed polarization (eq. 39,40) that was applied as a constraint. The models with $b/a = \sqrt{2}$ (solid curve) and 2 (broken curve) nearly coincide in this plot.

Studies of many sightlines (Serkowski et al. 1975) find that

$$p_{\text{max}} \lesssim 0.09E(B - V)/\text{mag} \quad (42)$$

or

$$p_{\text{max}} \lesssim 0.028A(\lambda_{\text{max}})/\text{mag} \quad (43)$$

Sightlines with $p_{\text{max}}/A(\lambda_{\text{max}}) < .028/\text{mag}$ are assumed to pass through regions where the magnetic field direction is not transverse to the line-of-sight, or varies along the sightline, or where the degree of grain alignment is for some reason lower than average.

5.2. Models With Partially-Aligned Dust Grains

We model the dust as a mixture of carbonaceous particles (including PAHs) and amorphous silicate particles. Models of the infrared emission from interstellar dust (Li & Draine 2001) require a population of PAH particles containing $C_{\text{PAH}}/H_{\text{total}} \approx 30 - 60\text{ppm}$. The present models assume PAHs to be present with a $C_{\text{PAH}}/H_{\text{total}} \approx 55\text{ppm}$, with optical properties as described by Li & Draine (2001). In order to reproduce the observed wavelength-dependent extinction, larger grains composed of both amorphous silicates and carbonaceous materials are required (e.g., Mathis, Rumpl, & Nordsieck 1977; Draine & Lee 1984; Weingartner & Draine 2001; Zubko, Dwek, & Arendt 2004). The carbonaceous particles are here taken to be spherical or randomly-oriented (and therefore not contributing to polarization), and the silicate particles are assumed to be spheroids, with diameter $2a$ along the symmetry axis, and $2b$ perpendicular to the symmetry axis. The size of a spheroid will be characterized by $a_{\text{eff}} \equiv (ab^2)^{1/3}$.

For the spherical carbonaceous grains, the IR to UV extinction was calculated using Mie theory, using the dielectric tensor of graphite with the usual 1/3-2/3 approximation (Draine & Malhotra 1993). For the silicate grains, taken to be oblate spheroids, we use the extended boundary condition method (EBCM) introduced by Waterman (1971) and developed by Mishchenko & Travis (1994) and Wielaard et al (1997) – see the general review by Mishchenko, Travis & Mackowski (1996). Our computations make use of the code `amp1d.lp.f` (Mishchenko 2000).⁴ EBCM codes encounter computational difficulties when the target becomes large compared to the wavelength. For the silicate oblate spheroids considered here, the `amp1d.lp.f` code appeared to converge for $b/\lambda < 3.88$, but sometimes failed for larger values of b/λ . Thus for $b/\lambda < 3.88$ we used `amp1d.lp.f` to calculate Q_{ext} for different orientations, but took

$$Q_{\text{ext}}(b/\lambda, b/a, m) \approx Q_{\text{ext}}(3.88, b/a, m) \quad \text{for } b/\lambda > 3.88 \quad . \quad (44)$$

For large values of b/λ , and for refractive indices appropriate to the optical and ultraviolet, the extinction tends to be close to twice the projected geometric cross section (with zero contribution to polarization of starlight in this limit). For the size distributions characteristic of interstellar grains, grains with $b/\lambda > 3.88$ make only a minor contribution to the total extinction, and a very small contribution to the polarization of starlight, so the approximation (44) does not introduce significant error.

We consider models where all the silicate particles are oblate⁵ ($b > a$) spheroids with a single axial ratio b/a , independent of size. The degree of alignment of grains of size a_{eff} is given by an alignment fraction $f(a_{\text{eff}})$; $0 \leq f \leq 1$, where $f = 0$ for random alignment, and $f = 1$ for grains where

⁴`amp1d.lp.f` is available at http://www.giss.nasa.gov/~crmim/t_matrix.html

⁵There is some indication that oblate shapes provide a better match to polarization observations (Draine & Lee 1984). Oblate spheroids also have the advantage of being invariant under rotation about their principal axis of largest moment of inertia, thus eliminating the need for averaging over grain rotation.

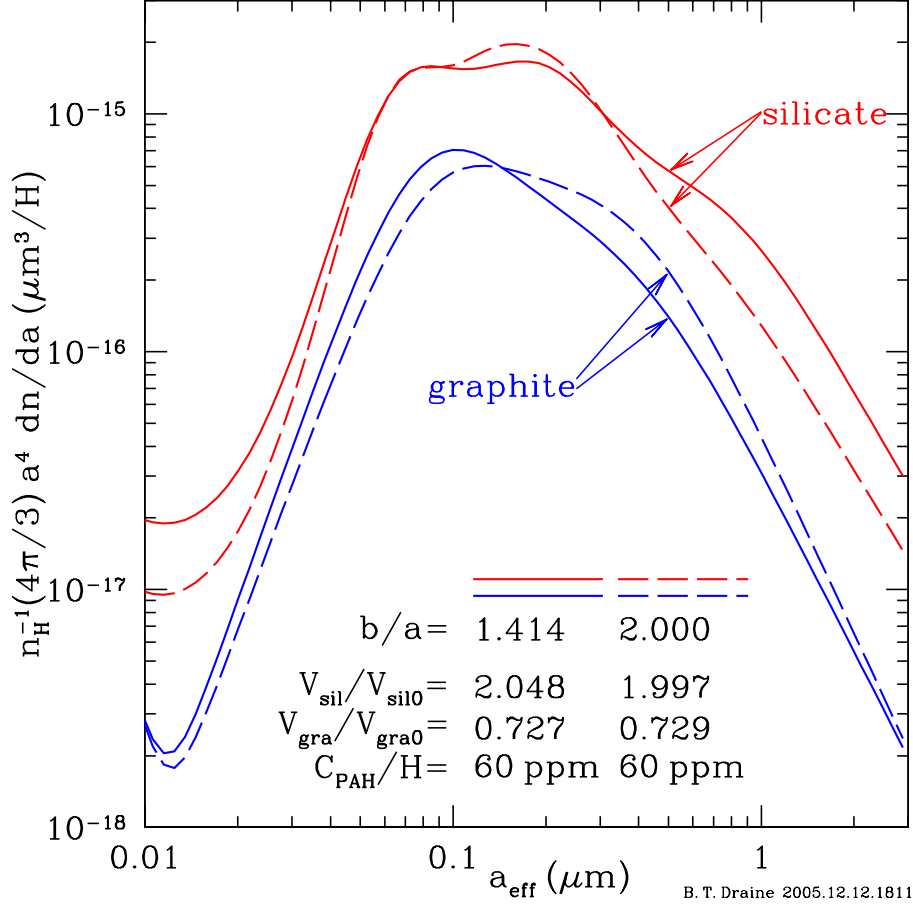


Fig. 9.— Size distributions for carbonaceous spheres and amorphous silicate oblate spheroids. Size distributions are constrained to be smooth, and to reproduce the observed extinction and polarization. The size distributions shown employ about twice as much silicate material as would be permitted by current estimates of solar abundances. The size distributions are not shown for $a_{\text{eff}} < 0.01\mu\text{m}$, because those grains contribute negligibly to X-ray scattering.

the short axis ($\hat{\mathbf{a}}_1$) is perfectly-aligned with the magnetic field direction. We assume the magnetic field to be perpendicular to the line-of-sight, and for simplicity we approximate the distribution of partially-aligned grains using “picket fence alignment”: if the line-of-sight is in the $\hat{\mathbf{z}}$ direction, and the magnetic field is in the $\hat{\mathbf{x}}$ direction, we assume that a fraction $(1+2f)/3$ of the oblate spheroids have $\hat{\mathbf{a}}_1 \parallel \hat{\mathbf{x}}$, $(1-f)/3$ have $\hat{\mathbf{a}}_1 \parallel \hat{\mathbf{y}}$, and $(1-f)/3$ have $\hat{\mathbf{a}}_1 \parallel \hat{\mathbf{z}}$. This is not a physically realistic distribution – as discussed in §3, one should properly integrate over some distribution function $\phi(\Theta_{\mathbf{B}\mathbf{J}})$ for the angle between the grain angular momentum \mathbf{J} and the magnetic field direction \mathbf{B} . However, given our lack of knowledge of the functional form of $\phi(\Theta_{\mathbf{B}\mathbf{J}})$, it is reasonable to assume picket-fence alignment, with a single number $f(a)$ characterizing the alignment of grains of size a .

We carry out a nonlinear least-squares fit for three continuous functions: the size distributions $(dn/da)_{\text{car}}$ and $(dn/da)_{\text{sil}}$ for carbonaceous grains and silicate grains, and the alignment function

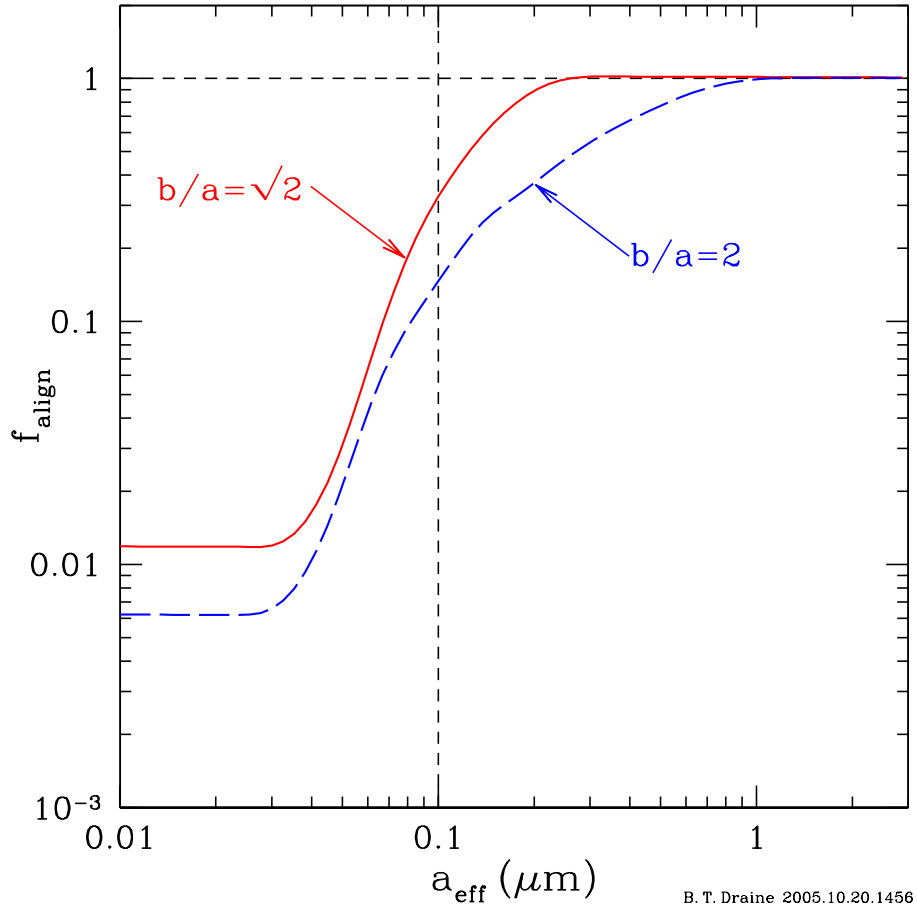


Fig. 10.— Fractional alignment for oblate silicate spheroids, as a function of effective radius a_{eff} . Large grains are perfectly aligned, with their principal axis of largest moment of inertia parallel to the local magnetic field direction. Small grains are only minimally aligned.

$f(a_{\text{eff}})$. This fit is carried out using a number of constraints, embodied in a penalty function $P = \sum_j (\Psi_j)^2$ that we seek to minimize. One of the constraints is the requirement that $p_{\text{max}}/A(\lambda_{\text{max}}) = .028/\text{mag}$, with $p(\lambda)/p_{\text{max}}$ required to reproduce eq. (39,40).

In addition to a penalty for deviations from the observed extinction and polarization (at 100 wavelengths, logarithmically spaced from $\lambda = 2.5\mu\text{m}$ to $\lambda = 0.111\mu\text{m}$), the penalty function P includes terms that are designed to favor solutions for which the size distributions dn_c/da and the alignment function $f(a)$ are smooth functions of a . In addition, the penalty function includes a term designed to favor alignment functions $f(a)$ with $df/da \geq 0$, as it is expected that small grains will be disaligned because of the effects of “thermal flipping” (Lazarian & Draine 1999a), while starlight torques (Draine & Weingartner 1997) will allow large grains to overcome the effects of thermal flipping and achieve suprathreshold rotation, resulting in efficient alignment of large grains with the interstellar magnetic field in diffuse regions.

In addition, we include a penalty if the size distribution uses more than the amount of silicate and carbon that would be present in solid form in the ISM if the total interstellar abundances of C, Mg, Si, and Fe were equal to current estimates of solar abundances. Because we have no accepted theoretical expectation for either the size distributions dn/da or the alignment function $f(a)$, the form of the penalty terms, and the weights they are given, are necessarily somewhat arbitrary. Our adopted penalty function P is described in the Appendix.

Kim & Martin (1995) modeled the polarization of starlight as a function of wavelength using silicate spheroids. For oblate spheroids with axial ratio $b/a = \sqrt{2}$, they found that the polarization can be explained if the grains with $a_{\text{eff}} \gtrsim 0.1\mu\text{m}$ are nearly perfectly aligned, in which case a sightline perpendicular to \mathbf{B} will have polarization $p_{\text{max}}/A_V \approx 0.028/\text{mag}$, the maximum value of the ratio observed in the interstellar medium. For larger values of b/a , only partial alignment of the $a \gtrsim 0.1\mu\text{m}$ silicate grains is required to produce the observed polarization.

Following Kim & Martin we take the silicate grains to be oblate spheroids with axial ratio $b/a = \sqrt{2}$, and we find the size distributions $(dn/da)_{\text{car}}$ and $(dn/da)_{\text{sil}}$ and alignment function $f(a_{\text{eff}})$ giving the best agreement with the observational constraints. We repeat this exercise for silicate grains with $b/a = 2$.

Figure 7 shows the extinction calculated for the two dust mixtures, together with the observed extinction. Figure 8 shows the polarization as a function of wavelength for the model, as well as the observed polarization. Both models successfully reproduce the observed extinction and polarization. However, in order to do so, both models require about twice as much silicate material as would be allowed by current estimates for the solar abundances of Mg, Si, and Fe. Sofia & Meyer (2001) recently discussed the applicability of solar abundances to the interstellar medium, and argue that abundances in young F and G stars provide a better standard, with Mg/H and Si/H about 12% and 23% above the values currently favored for the Sun (although the Mg and Si abundances in F and G stars have large uncertainties – 40% and 33%, respectively), but this is still less than the amount of Mg and Si required to reproduce the observed extinction and polarization for the grain model considered here. This abundance shortfall is generally encountered by models that use “compact” grains to reproduce interstellar extinction (e.g., Weingartner & Draine 2001). It may indicate that the abundances of interstellar Mg and Si are higher than estimated from either the Sun or young F and G stars. Alternatively, it may indicate that interstellar grains have other geometries, e.g., “composite” grains with vacuum fractions of order 50% or more (e.g., Zubko et al. 2004), which might permit the observed extinction to be accounted for using less material in grains.

In Figure 9 we show the best-fit size distributions of silicate and carbonaceous grains. Figure 10 shows the best-fit fractional alignment $f(a_{\text{eff}})$. As previously found by Kim & Martin, silicate grains with $b/a = \sqrt{2}$ must be nearly perfectly aligned for $a_{\text{eff}} \gtrsim 0.2\mu\text{m}$ if the observed polarization is to be reproduced.

6. X-Ray Scattering from Partially Aligned Interstellar Grains

6.1. Dust at a Single Distance

We have calculated the X-ray scattering properties of graphite and silicate dust grains with the size distributions and fractional alignments shown in Figs. 9 and 10, for 3 X-ray energies: $E = 0.5$, 1, and 2 keV. The total scattering cross section σ_{sca} is given in Table 1 for the two partially-aligned grain models, for two viewing directions: $\mathbf{z} \parallel \mathbf{B}$ and $\mathbf{z} \perp \mathbf{B}$. The two models have similar values of σ_{sca} – the total strength of X-ray scattering does not appear to discriminate between grain models with different degrees of grain elongation, if the models are already constrained to reproduce the observed optical extinction and polarization.

Also shown in Table 1 are X-ray scattering cross sections calculated for a graphite+silicate grain model for spherical grains with the size distribution adopted by Weingartner & Draine (2001; hereafter WD01). The WD01 size distribution is based on using graphite and silicate spheres plus PAH molecules to reproduce the observed interstellar extinction from the infrared to the ultraviolet; the resulting size distribution differs in detail from what is found here for spheroids constrained to also reproduce the polarization of starlight, but the total X-ray scattering cross sections σ_{sca} are very similar to those obtained here for spheroidal grains.

The ratio of X-ray scattering to visual extinction, τ_{sca}/A_V , is plotted in Fig. 11 for both the present models and the WD01 model, together with observational determinations. Aside from the apparent agreement between model and observation for the soft X-rays from Nova Cyg 1992 (Draine & Tan 2003), there appears to be a general tendency for the observationally-determined X-

Table 1. Total X-Ray Scattering Cross Section σ_{sca} (10^{-24} cm²/H)^a

Model	Orientation	$E = 0.5$ keV	$E = 1$ keV	$E = 2$ keV
$b/a = 1.414$	$\mathbf{z} \perp \mathbf{B}$	163.	90.2	38.7
“	$\mathbf{z} \parallel \mathbf{B}$	153.	82.1	32.5
“	random	160.	87.5	36.7
$b/a = 2.000$	$\mathbf{z} \perp \mathbf{B}$	172.	96.9	40.2
“	$\mathbf{z} \parallel \mathbf{B}$	145.	75.8	26.6
“	random	163.	89.9	35.7
WD01 model ^b	random	173.	89.7	29.8

^a $\tau_{\text{sca}}/A_V = (N_{\text{H}}/A_V) \times \sigma_{\text{sca}}$, with $N_{\text{H}}/A_V \approx 1.87 \times 10^{21}$ cm²/mag (Bohlin et al. 1978).

^b $R_V = 3.1$, $C_{\text{PAH}}/\text{H} = 55$ ppm

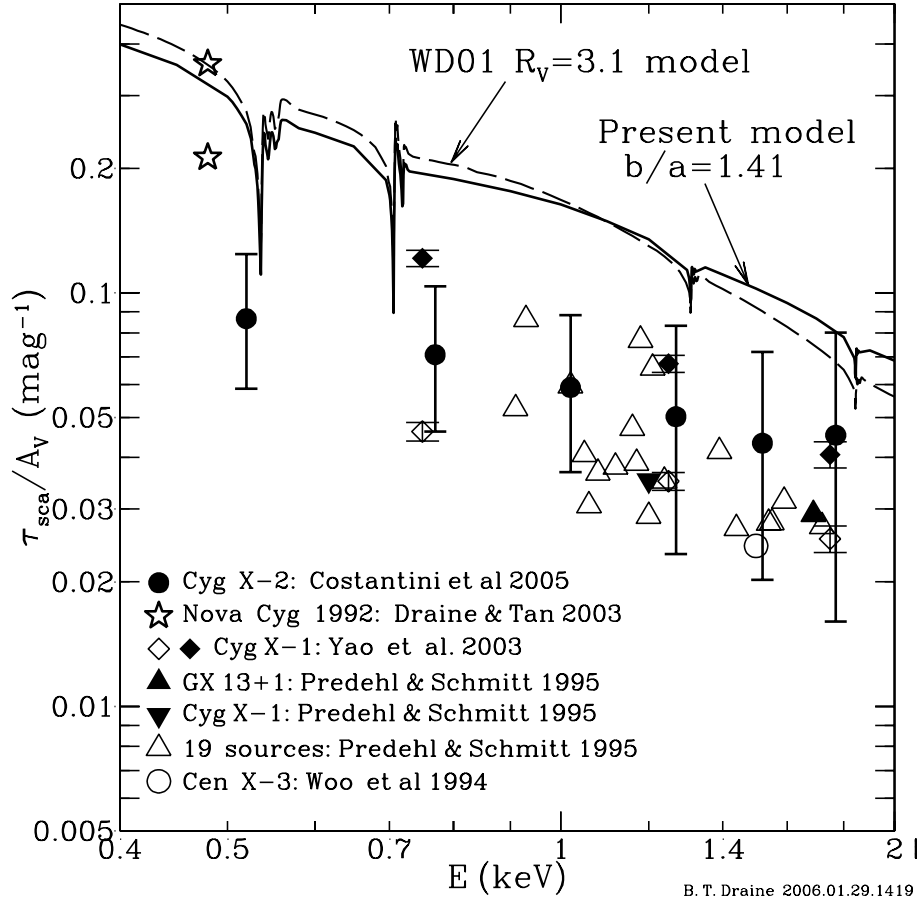


Fig. 11.— τ_{sca}/A_V vs. energy E , where τ_{sca} is the total optical depth for scattering, and A_V is the visual extinction. Solid curve: scattering calculated for the present size distributions for graphite spheres and silicate spheroids (randomly-oriented) with $b/a = 1.414$ (results for $b/a = 2$, not shown, are nearly identical). Broken curve: scattering calculated for graphite and silicate spheres with the WD01 size distribution. Also shown are observational results. For the Cyg X-1 observations by Yao et al. (2003), the filled diamonds are corrected for scattering at $\theta > 120''$ (see Draine 2003b). For Nova Cyg 1992, results are shown for $\tau_{\text{sca}} = 0.21$ (Draine & Tan 2003) and two estimates of $E(B - V)$: 0.19 mag (Mathis et al. 1995) and 0.32 mag (Vanlandingham et al. 2005).

ray τ_{sca}/A_V to be smaller than predicted by grain models based on mixtures of solid carbonaceous grains and solid silicate grains. However, measuring the X-ray scattering by dust is difficult at small angles, where it is mixed with the point spread function, and at large angles, where background corrections are uncertain. At this time we consider the current grain model to be viable, despite the fact that most of the observational data in Fig. 11 appears to fall significantly below the prediction. Definitive measurement of the total X-ray scattering cross section per unit A_V would be of great value.

The total scattering cross sections given in Table 1 appears to decrease by $\sim 6-35\%$, depending

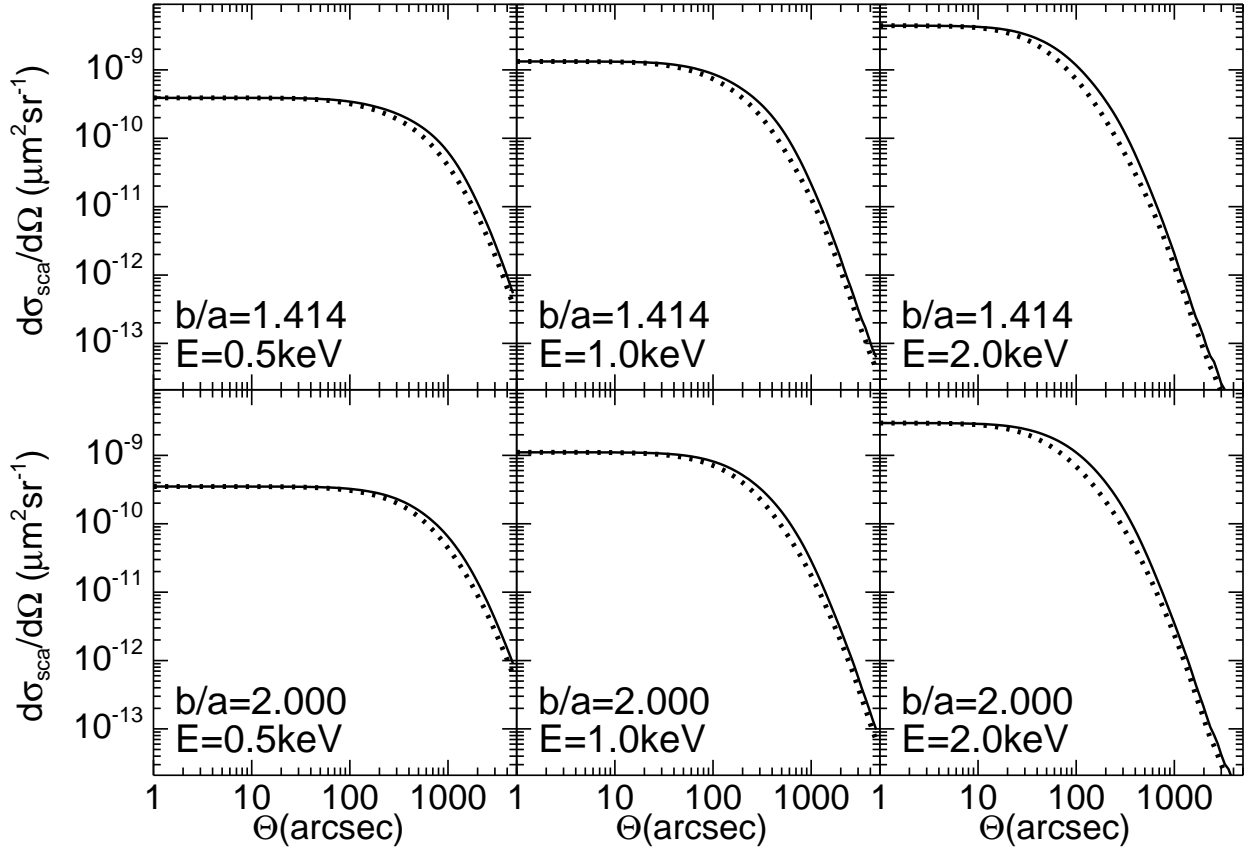


Fig. 12.— Differential scattering cross sections per H nucleon vs. scattering angle Θ for the grain mixtures of Fig. 9 at $\phi = 0$ (solid line) and $\phi = \pi/2$ (dotted line). Results are shown for $E = 0.5, 1, 2$ keV, and for silicate grain axial ratio $b/a = \sqrt{2}$ and $b/a = 2$. For optically-thin scattering by dust at a single distance, the halo intensity $I(\theta, \phi) \propto d\sigma/d\Omega(\Theta, \phi)$, where $\Theta = \theta/\zeta$ for $\zeta \equiv z/D$, where z is the distance from the source to the dust and D is the distance from the source to the observer.

on energy and b/a , when the viewing angle is changed from $\mathbf{z} \perp \mathbf{B}$ (maximum optical polarization) to $\mathbf{z} \parallel \mathbf{B}$ (zero optical polarization). This small effect would probably be difficult to confirm observationally.

Fig. 12 shows the differential scattering cross section per H nucleon as a function of scattering angle θ , for $\phi = 0$ and $\phi = 90^\circ$, assuming the magnetic field to be in the $\hat{\mathbf{x}}$ direction ($\phi = 0$). For $\theta > 0$, the scattering is stronger for $\phi = 0$ (the direction of the short axis of the aligned grains), but the differences between $\phi = 0$ and $\phi = 90^\circ$ are of course reduced compared to the single-grain results in Fig. 2 because we are averaging over an extended size distribution, and except for the largest grains, there is only partial grain alignment. Nevertheless, the differences can be as large as $\sim 40\%$ at $\theta \gtrsim 200(\text{keV}/E)$ arcsec.

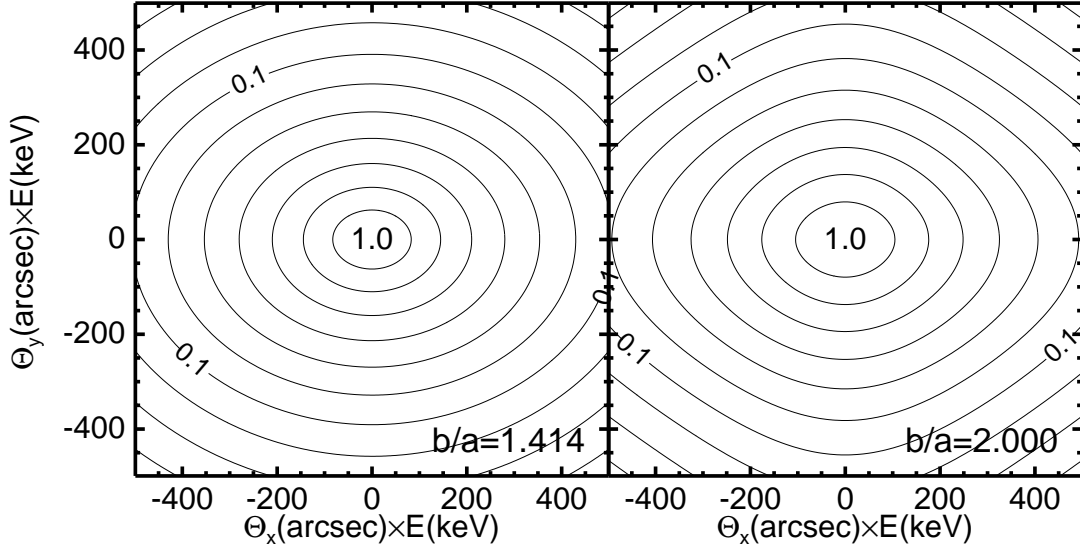


Fig. 13.— Contours of constant $\bar{\sigma}(\Theta, \phi)/\bar{\sigma}(0, 0) = 10^{-n/7}$ for $E = 1$ keV for grain models including partially-aligned silicate grains with $b/a = \sqrt{2}$ and 2, for magnetic field $\mathbf{B} \parallel \hat{\mathbf{x}}$.

Fig. 14 shows the anisotropy measures $R_2^{(\sigma)}(0, \theta)$ and $R_4^{(\sigma)}(0, \theta)$ for the partially-aligned grain models with $b/a = \sqrt{2}$ and 2. Note that, for fixed θE , the anisotropy measures R_2 and R_4 are larger at higher energies. The higher Z elements in the silicate grains (versus $Z = 6$ for the carbon grains) cause $|m - 1|$ to decline less rapidly with energy than for carbon grains; as a result, the silicate grains provide an increasing fraction of the total scattering as the energy is increased. Since the silicate grains are aligned, but the carbon grains are not, the anisotropy measures R_2 and R_4 therefore increase with increasing E .

The top panel of Fig. 14 shows $g(0, \Theta)$, the fraction of the scattered power having scattering angles $< \Theta$, calculated for $E = 0.5, 1, 2$ keV and the grain models for $b/a = \sqrt{2}$ and 2. If the dust is located at a single distance D_d from the observer, not too close to the source, the anisotropy measures of the observed halo are directly related to the anisotropy measures $R_\ell^{(\sigma)}$ of the dust mixture:

$$R_\ell^{(I)}(\theta_1, \theta_2) = R_\ell^{(\sigma)}\left(\frac{\theta_1}{\zeta}, \frac{\theta_2}{\zeta}\right) \quad (45)$$

where $\zeta = (D - D_d)/D$, where D_d is the distance of the dust from the observer. Thus far we have been considering scattering by dust at a single distance. This will apply, for example, if most of the dust on the line-of-sight to the source is concentrated in a single cloud and the source-cloud distance was large compared to the extent of the cloud along the line-of-sight. It also applies to scattering by Galactic dust of photons from an AGN, QSO, or GRB, in which case $\zeta \rightarrow 1$.

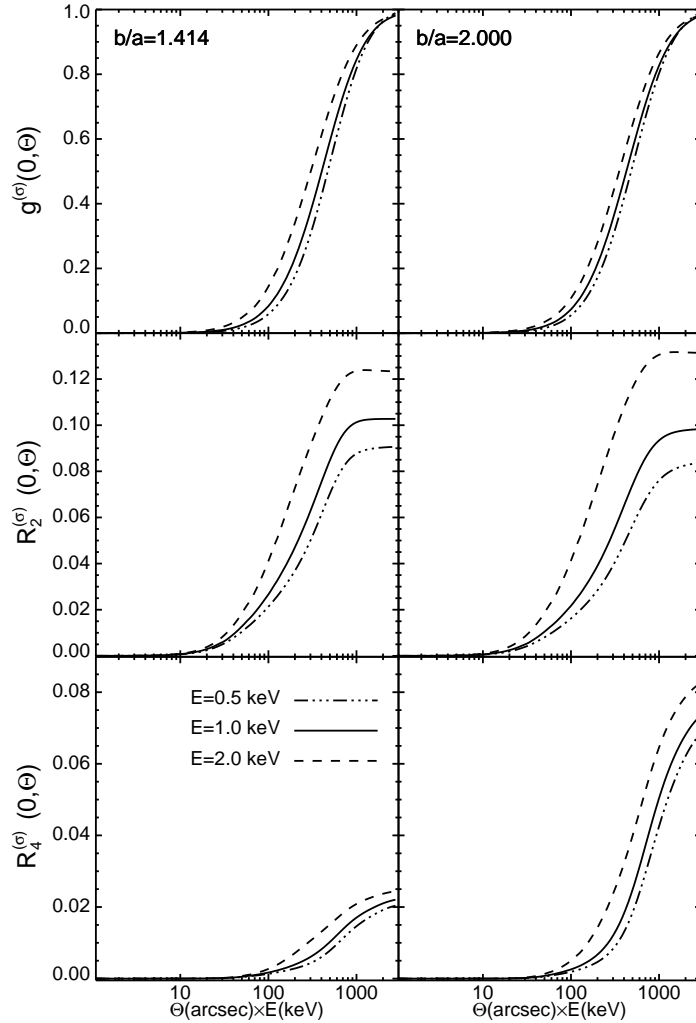


Fig. 14.— $R_2^{(\sigma)}(0, \Theta)$ and $R_4^{(\sigma)}(0, \Theta)$ vs. ΘE for dust mixtures with realistic size distributions and degree of alignment. For grains in a sheet at a distance $(1 - \zeta)D$ from the observer, where D is the distance to the source, $R_n^{(I)}(0, \theta) = R_n^{(\sigma)}(0, \theta = \zeta\Theta)$, where θ is the observed halo angle. Results for $E = 0.5, 1, 2$ keV are shown for grain models where the silicate grains are oblate spheroids with axial ratios $b/a = \sqrt{2}$ and 2.

6.2. Uniformly-Distributed Dust

If the dust is distributed between the observer and the source, the scattering halo depends on the specific dust distribution. As a simple example, we consider dust with uniform density for $0.01 \leq z/D \leq 1$, with zero density for $z < .01D$.⁶

⁶The dust-free zone near the source is introduced in order to keep $I(0, 0)$ finite. For dust uniformly-distributed all the way to the source, it can be seen that $I(\theta, \phi) \propto \theta^{-1}$ for $\theta \rightarrow 0$. This divergence is of little practical consequence,

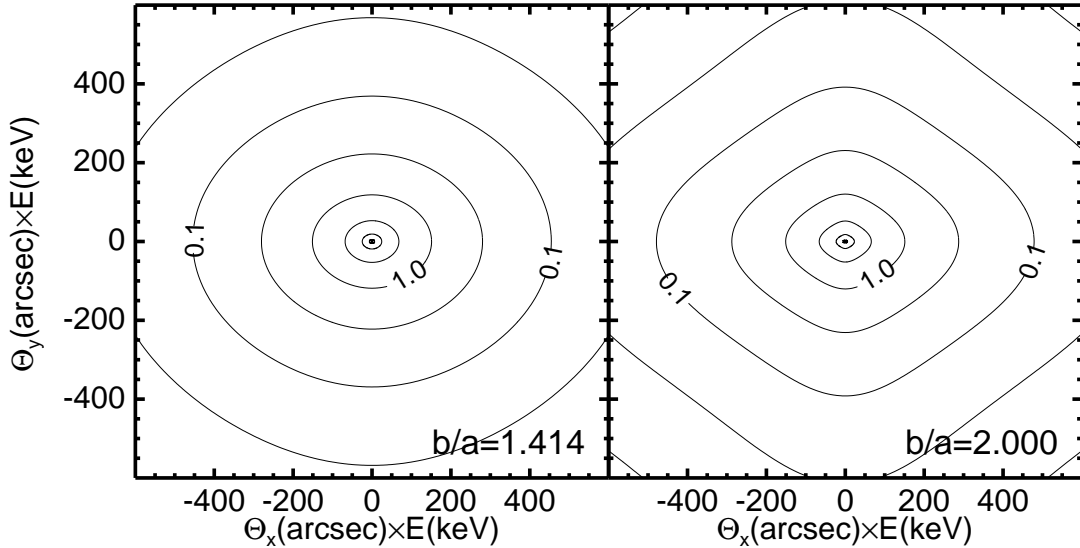


Fig. 15.— Contours of constant $I(\theta, \phi)/I(\theta_N, 0) = 10^{-n/2}$, for $\theta_N \equiv 150''$, for uniformly-distributed mixture of partially-aligned grains if silicate grains have axial ratio (a) $b/a = \sqrt{2}$; (b) $b/a = 2$. Contours are labelled by $I/I(\theta_N, 0)$. Contours plotted are for $E = 1$ keV; for other energies, the halo intensities can be estimated from the approximate scaling relation $\bar{\sigma}(E, \Theta) \approx \bar{\sigma}(1 \text{ keV}, \Theta E/\text{keV})$

Fig. 15 shows contours of scattered intensity for this case. In contrast to Fig. 4, the iso-intensity contours are no longer perfect ellipses for this case, as the result of the scattering contributions from the carbon spheres and nonaligned silicate spheroids. Nevertheless, it is seen that the iso-intensity contours are noticeably noncircular. Fig. 16 shows the normalized scattered intensity in the $\phi = 0$ and $\phi = 90^\circ$ directions for the two partially-aligned mixtures.

The anisotropy measures $R_2^{(I)}(\theta_1, \theta_2)$ and $R_4^{(I)}(\theta_1, \theta_2)$ for uniformly-distributed partially-aligned dust are shown in Fig. 17, for the two values of b/a . Results are shown for a number of choices of θ_1 , the inner radius of the annulus over which $I(\theta, \phi)$ is assumed to be measured. The function $g(\theta_1, \theta_2)$, shown in the top panel, gives the fraction of the total scattered power that falls in the annulus $[\theta_1, \theta_2]$. The observer will want to ensure that the chosen annulus $[\theta_1, \theta_2]$ will have enough scattered signal in it to allow reliable determination of the moment R_2 and, ideally, R_4 .

because the enclosed power $\int_0^\theta I 2\pi\theta' d\theta' \rightarrow 0$ as $\theta \rightarrow 0$.

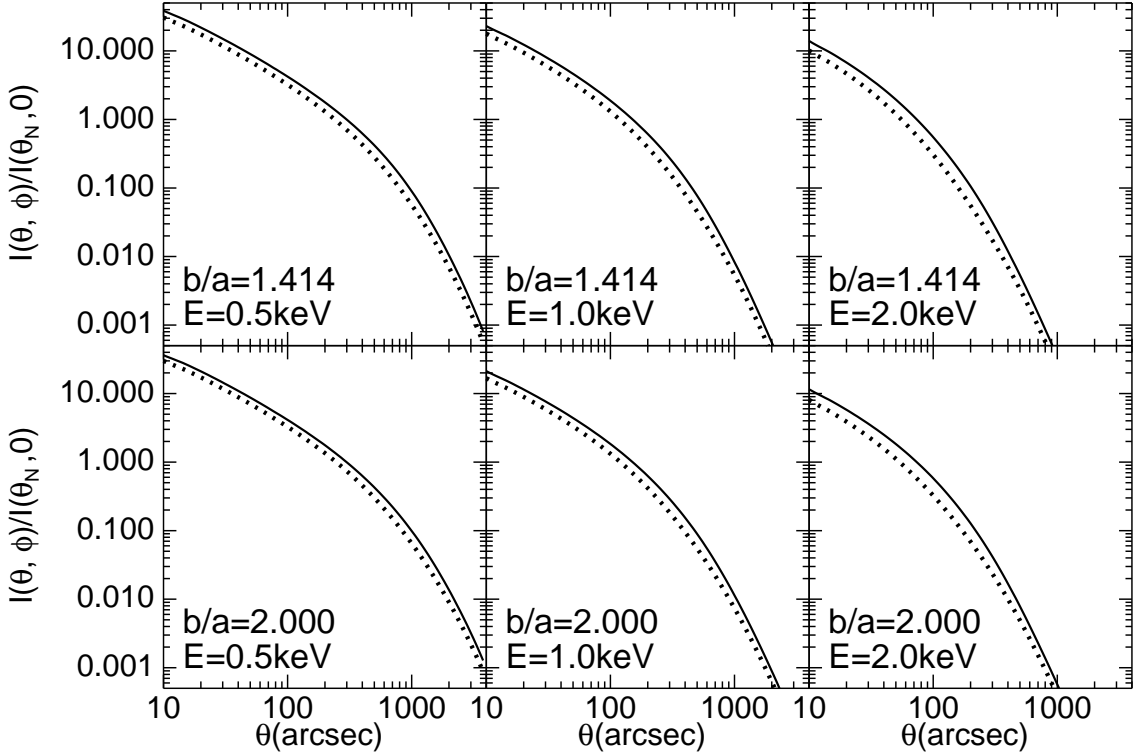


Fig. 16.— $I(\theta, \phi)/I(\theta_N, 0)$ vs. θ for $\phi = 0$ (solid curve) and $\phi = \pi/2$ (dotted curve) for uniformly-distributed grains at $E = 0.5, 1, 2$ keV, for assumed silicate axial ratio $b/a = \sqrt{2}$ and $b/a = 2$. The arbitrary normalization point $\theta_N \equiv 150 \text{ arcsec}/E(\text{keV})$.

7. Discussion

7.1. Observational Considerations

We will assume that there is no uncertainty regarding the position of the point source on the sky; this position is taken to be the origin of a polar coordinate system $(\theta, \phi_{\text{obs}})$ with the direction of $\phi_{\text{obs}} = 0$ taken to be whatever coordinate system is convenient to the observer. We further assume that the image $I(\theta, \phi_{\text{obs}})$ has had the instrumental point spread function (p.s.f.) subtracted; this is especially important if the p.s.f. is not azimuthally symmetric. Real images may contain extraneous background or foreground sources that need to be recognized and removed; we assume that standard methods are used to interpolate the scattered intensity $I(\theta, \phi_{\text{obs}})$ in such regions. In the following discussion it is assumed that $I(\theta, \phi_{\text{obs}})$ is the observed scattered intensity.

An annulus $[\theta_1, \theta_2]$ is chosen that contains a strong scattered signal, with θ_1 chosen to avoid the central core that will be dominated by the instrumental p.s.f., and θ_2 chosen to ideally extend beyond the radius where the scattered halo intensity begins to significantly decline. If $I(\theta, \phi_{\text{obs}})$ is the

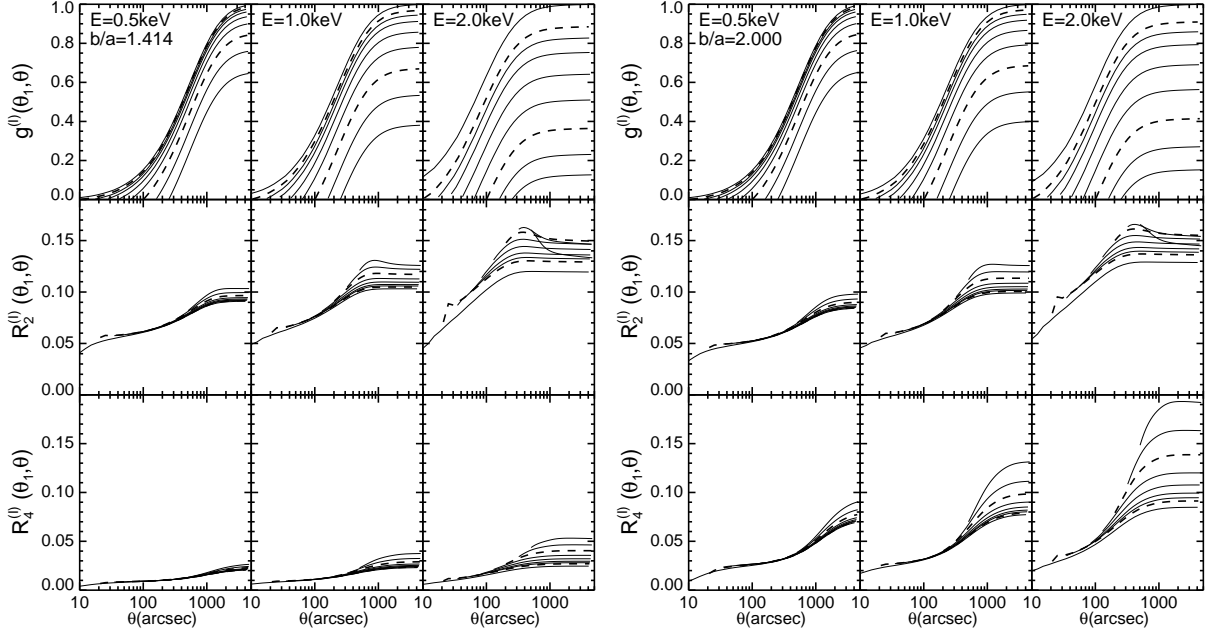


Fig. 17.— $g^{(I)}(\theta_1, \theta)$, the fraction of the scattered energy in the annulus $[\theta_1, \theta]$, and the asymmetry parameters $R_2^{(I)}(\theta_1, \theta)$ and $R_4^{(I)}(\theta_1, \theta)$ vs. θ for the annulus $[\theta_1, \theta]$, for grains uniformly-distributed between observer and source, for $E = 0.5, 1, 2$ keV, and where the silicate grains have been assumed to have axial ratio $b/a = \sqrt{2}$ and 2.

b

observed intensity (corrected for nonuniform backgrounds), a new coordinate system $\phi \equiv \phi_{\text{obs}} - \Delta$ is defined, with the rotation angle Δ determined by the condition

$$\Delta = \frac{1}{2} \arctan(A/B) \quad , \quad (46)$$

$$A \equiv \int_{\theta_1}^{\theta_2} d\theta \sin \theta \int_0^{2\pi} d\phi_{\text{obs}} I(\theta, \phi_{\text{obs}}) \sin(2\phi_{\text{obs}}) \quad , \quad (47)$$

$$B \equiv \int_{\theta_1}^{\theta_2} d\theta \sin \theta \int_0^{2\pi} d\phi_{\text{obs}} I(\theta, \phi_{\text{obs}}) \cos(2\phi_{\text{obs}}) \quad . \quad (48)$$

$$(49)$$

In this coordinate system (θ, ϕ) , the anisotropy statistics $R_\ell^{(I)}(\theta_1, \theta_2)$ can be calculated from eq. (36). The resulting $R_2^{(I)}(\theta_1, \theta_2)$ and $R_4^{(I)}(\theta_1, \theta_2)$ can be compared to the theoretical predictions in Figure 14 (for dust at a single distance) or Figure 17 (for uniformly-distributed dust).

We have calculated the anisotropy statistics $R_\ell^{(I)}$ for plane-parallel distributions of dust: dust in a sheet at a single distance and dust uniformly distributed between observer and source. In real situations, gradients in the dust density distribution perpendicular to the line-of-sight (on linear scales of order $\theta_{\text{halo}} \approx 1' \times 1 \text{ kpc} \approx 0.3 \text{ pc}$) can contribute to the $R_\ell^{(I)}$. How can halo anisotropies due to aligned dust grains be separated from anisotropies due to dust density gradients?

1. The halo anisotropy due to dust grain alignment will have $R_1^{(I)} = R_3^{(I)} = 0$. Dust density gradients, on the other hand, will generally contribute to all of the $R_\ell^{(I)}$, and in fact would be expected to make the largest contribution to $R_1^{(I)}$. Therefore the magnitude of $R_1^{(I)}$ and $R_3^{(I)}$ can be used to estimate the contribution of dust density gradients to $R_2^{(I)}$.
2. The halo anisotropy due to aligned dust grains will be aligned with the direction of starlight polarization: polarized starlight has \mathbf{E} parallel to the short axis of the aligned grains. Therefore the scattered halo will have its major axis parallel to the direction of starlight polarization: the angle Δ should coincide with the direction of starlight polarization.
3. If the anisotropic signal $R_2^{(I)}$ is from aligned grains, the angle Δ will be insensitive to the choice of annulus $[\theta_1, \theta_2]$. If Δ is found to vary significantly from one annulus to another, the observed anisotropy will have an appreciable component from some source other than aligned dust grains. – nonuniform dust, or other X-ray sources in the field.

Ideally, the X-ray scattering halo would be observed for a source where the optical starlight polarization is known either for the source itself or a nearby stellar companion. In some cases, the X-ray source may not be bright enough at optical wavelengths to permit polarization measurements. However, the polarization of starlight is known to display large-scale coherence over the sky (see, e.g., Mathewson & Ford 1970); therefore if starlight polarization has been observed for a star that is nearby on the sky, with a similar amount of reddening, it is reasonable to presume that the dust in front of the candidate X-ray source would produce a similar degree of optical polarization.

Directions with large observed starlight polarization tend to lie close to the galactic plane (so that significant amounts of reddening will be present) and in directions perpendicular to the general direction of the local magnetic field. An example of a region with large observed starlight polarization per unit $E(B - V)$ is $l = 130 \pm 10$ deg. Figure 18 shows $p(V)/E(B - V)$ for stars in a section of the Galactic plane near $l \approx 130$ deg. The stars shown are limited to $0.30 \leq E(B - V) \leq 0.60$ mag (i.e., $0.9 \lesssim A_V \lesssim 1.9$ mag). The large-scale coherence of the polarization direction is apparent, and it is also evident that the ratio of polarization to reddening is relatively uniform. This indicates that the magnetic field is relatively well-ordered, and that the efficiency of grain alignment is also relatively uniform. An X-ray source in this general region would presumably be observed through the same aligned dust as the stars for which the polarization has already been measured.

7.2. Predictions

We have considered two models for interstellar grains, both with partially aligned silicate oblate spheroids, but for two different axial ratios. The aligned grains that produce polarization of starlight also produce anisotropic X-ray scattering. While we have explicitly calculated the anisotropic X-ray scattering only for the optimal case where the magnetic field \mathbf{B} is unidirectional

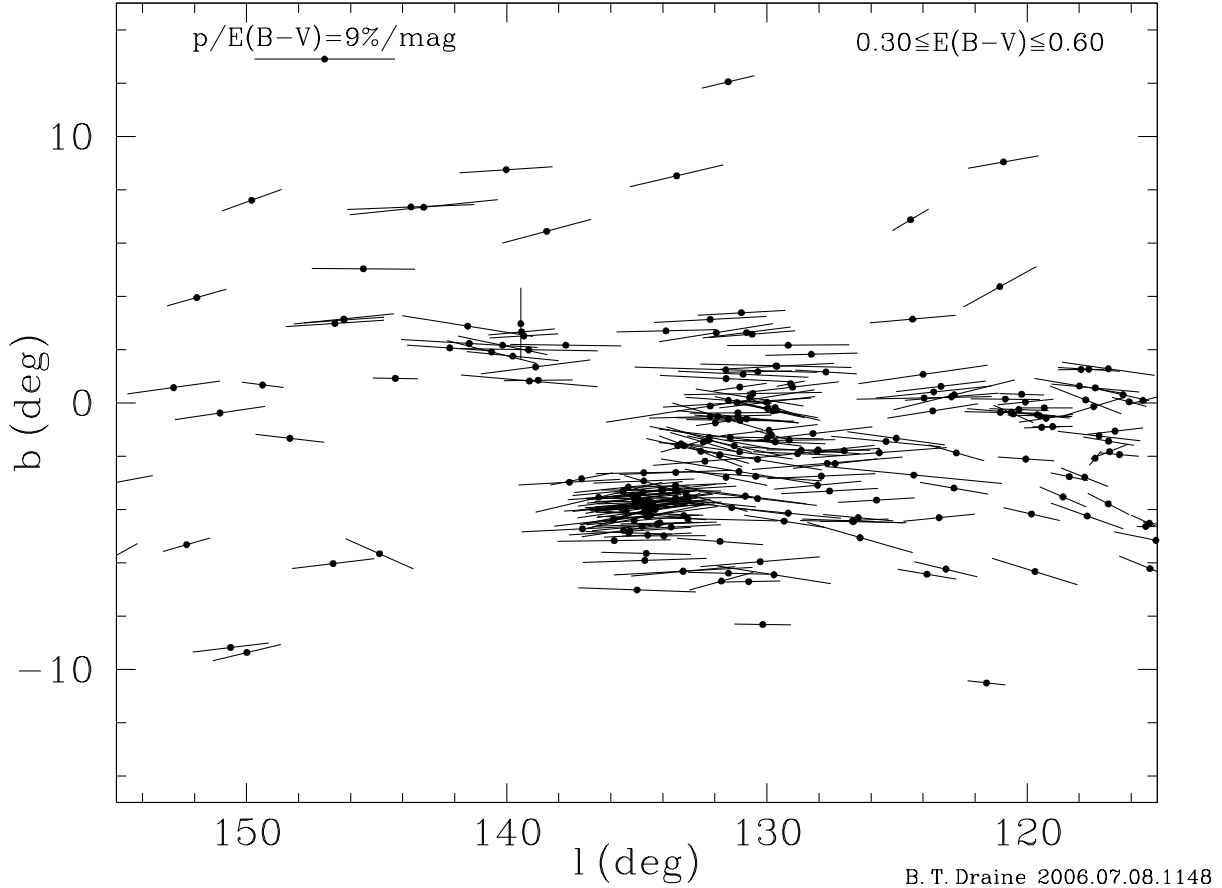


Fig. 18.— Line segments show ratio direction of starlight polarization, with length proportional to $p(V)/E(B-V)$, where $p(V)$ is the polarization, and $E(B-V)$ is the reddening. Data from Heiles (2000). In this region of the sky, the dust grain alignment is evidently quite uniform, and the polarization per unit $E(B-V)$ is $\sim 2/3$ of the empirical maximum.

and perpendicular to the line-of-sight, we expect that for other magnetic field geometries, the anisotropy $R_2^{(I)}$ will decrease in proportion to $p_{\max}/E(B-V)$, because for optically-thin conditions both $R_2^{(I)}$ and $p_{\max}/E(B-V)$ respond similarly to changes in the magnetic field direction.⁷ We can therefore predict the ratio of the fractional anisotropy of the X-ray halo to the ratio of the optical polarization to total reddening.

We suppose that it is possible to measure the X-ray halo for $\theta_1 < \theta < \theta_2$, with $\theta_1 \lesssim 200''$, and $\theta_2 \gtrsim 300''$. If the dust is distributed approximately uniformly between observer and source, from

⁷E.g., both are unchanged if $\mathbf{B} \rightarrow -\mathbf{B}$; both vanish if $\mathbf{B} \parallel \hat{\mathbf{z}}$; and both vanish if 50% of the dust has symmetry axis $\hat{\mathbf{a}}_1 \parallel \hat{\mathbf{x}}$, and 50% has $\hat{\mathbf{a}}_1 \parallel \hat{\mathbf{y}}$.

Figure 17 we see that for X-ray energy $E = 1$ keV,

$$R_2^{(I)}(\theta_1, \theta_2) \gtrsim 0.09 \times \left[\frac{p_{\max}}{0.09E(B - V)/\text{mag}} \right] , \quad (50)$$

provided the annulus has $\theta_1 \lesssim 300''$, and $\theta_2 \gtrsim 300''$. The two cases $b/a = \sqrt{2}$ and 2 give similar values for the quadrupole anisotropy $R_2^{(I)}$ – increased grain oblateness is offset by reduced degree of partial alignment. As discussed above, the anisotropy $R_2^{(I)}$ is an increasing function of energy over the range 0.5–2 keV because the relative contribution of the nonspherical silicate grains to the scattering increases with energy.

It is not critical that the dust be distributed uniformly for the result (50) to be applicable, only that a negligible amount of the starlight polarization be produced by dust that is very close to the source, as the anisotropic X-ray halo produced by this dust may be largely lost at small angles unless it is possible to use small values of θ_1 .

Aligned grains are also predicted to produce an octupole anisotropy in the X-ray halo, measured by $R_4^{(I)}$. Unfortunately, this anisotropy can be washed out by moderate rotation of the magnetic field direction along the line-of-sight. However, if the starlight polarization has $p_{\max} \approx 0.09E(B - V)/\text{mag}$, then we can suppose that the magnetic field in the dusty regions is approximately perpendicular to the line-of-sight and unidirectional (otherwise the net starlight polarization would be reduced). In this case, we can use the statistic $R_4^{(I)}$ as a test of grain models. The model with minimal axial ratio $b/a \approx 1.4$ for the spheroids predicts $R_4^{(I)} \approx 0.03$ at 1 keV (see Figure 17). If larger values of $R_4^{(I)}$ are observed, it will suggest more extreme grain shapes (for example, $R_4^{(I)} \approx 0.10$ would be consistent with $b/a \approx 2$ for the silicate spheroids, but inconsistent with $b/a \approx \sqrt{2}$). Therefore, measurement of $R_4^{(I)}$ has the potential to discriminate between grain models with different grain shape.

8. Summary

The principal results of this paper are as follows:

1. We show that anomalous diffraction theory can be used for accurate calculation of X-ray scattering from dust grains with arbitrary shape. Fast Fourier transforms may be employed for efficient calculation of the scattering halo.
2. Differential scattering cross sections are calculated for oblate spheroids, and are shown to have substantial anisotropies if the spheroid axial ratio differs appreciably from unity.
3. Models of spherical carbonaceous grains and partially-aligned silicate spheroids are found that reproduce the observed interstellar extinction and polarization of starlight as a function of wavelength. Confirming a result found previously by Kim & Martin (1995), we find that for silicate axial ratio $b/a \approx \sqrt{2}$ the model can reproduce the largest observed starlight

polarization, provided that the silicate spheroids with $a_{\text{eff}} \gtrsim 0.1\mu\text{m}$ are almost perfectly aligned (with their short axis parallel to the magnetic field). For larger axial ratios, the grain alignment need not be so complete.

4. X-ray scattering halos are calculated for aligned interstellar dust grains. For realistic size distributions and fractional alignments, the scattered halo shows substantial anisotropy.
5. We propose statistics $R_\ell^{(I)}(\theta_1, \theta_2)$ to measure the halo anisotropy in an annulus $\theta_1 < \theta < \theta_2$. We predict the values of $R_2^{(I)}/[p_{\text{max}}/E(B - V)]$. We find that $R_2^{(I)}$ is large enough to be measured on sightlines to X-ray point sources where the grains are aligned so as to produce starlight polarization with $p_{\text{max}}/E(B - V) \gtrsim 0.05/\text{mag}$.
6. We show that the octupole anisotropy $R_4^{(I)}$ is sensitive to the assumed grain shape. On favorable sightlines, $R_4^{(I)}$ can be used to constrain the geometry of interstellar grains.

This research was supported in part by NSF grants AST-0216105 and AST-0406883. We are grateful to an anonymous referee for helpful comments. B.T.D. is grateful to R. Bandiera for valuable discussions, and to R.H. Lupton for availability of the SM software package.

REFERENCES

- Asplund, M. 2000, *A&A*, 359, 755
- Asplund, M., Nordlund, Å, Trampedach, R., Allende Prieto, C., & Stein, R.F. 2000, *A&A*, 359, 729
- Asplund, M., Grevesse, N., Sauval, A.J., Allende Prieto, C., & Kiselman, D. 2004, *A&A*, 417, 751
- Asplund, M., Grevesse, N., Sauval, A.J., Allende Prieto, C., & Blomme, R. 2005, *A&A*, 431, 693
- Bohlin, R.C., Savage, B.D., & Drake, J.F. 1978, *ApJ*, 224, 132
- Bohren, C.F., & Huffman, D.R. 1983, *Absorption and Scattering of Light by Small Particles* (NY: Wiley).
- Catura, R.C. 1983, *ApJ*, 275, 645
- Costantini, E., Freyberg, M.J., & Predehl, P., *A&A*, 444, 187
- Debye, P. 1909, *Ann. Phys.*, 30, 57
- Draine, B.T. 2003a, *ARAA*, 41, 241
- Draine, B.T. 2003b, *ApJ*, 598, 1026

- Draine, B.T., & Lee, H.-M. 1984, *ApJ*, 285, 89
- Draine, B.T., & Malhotra, S. 1993, *ApJ*, 414, 632
- Draine, B.T., & Tan, J.C. 2003, *ApJ*, 594, 347
- Draine, B.T., & Weingartner, J.C. 1997, *ApJ*, 480, 633
- Frisch, P.C., Dorschner, J.M., Geiss, J., Greenberg, J.M., Grün, E., Landgraf, M., Hoppe, P., et al., 1999, *ApJ*, 525, 492
- Grevesse, N., & Sauval, A.J., 1998, *Sp. Sci. Rev.*, 85, 161
- Hall, J.S. 1949, *Science*, 109, 166
- Hayakawa, S. 1970, *Prog. Theor. Phys.*, 43, 1224
- Heiles, C. 2000, *AJ*, 119, 923
- Hiltner, W.A. 1949, *Science*, 109, 165
- Kim, S.-H., & Martin, P.G. 1995, *ApJ*, 442, 172
- Lazarian, A., & Draine, B.T. 1999a, *ApJ*, 516, L37
- Lazarian, A., & Draine, B.T. 1999b, *ApJ*, 520, L67
- Li, A., & Draine, B.T. 2001, *ApJ* 554, 778
- Martin, P.G., Adamson, A.J., Whittet, D.C.B., Hough, J.H., Bailey, J.A., Kim, S.-H., Sato, S., Tamura, M., & Yamashita, T. 1992, *ApJ*, 392, 691
- Mathewson, D.S., & Ford, V.L. 1970, *Mem. R. Astron. Soc.*, 74, 139
- Mathis, J.S., Cohen, D., Finley, J.P., & Krautter, J. 1995, *ApJ*, 449, 320
- Mathis, J.S., Ruml, W., & Nordsieck, K.H. 1977, *ApJ*, 217, 425
- Mauche, C.W., & Gorenstein, P. 1986, *ApJ*, 302, 371
- Mie, G. 1908, *Ann. Phys.* 25, 377
- Mishchenko, M.I. 2000, *Applied Optics*, 39, 1026
- Mishchenko, M.I., & Travis, L.D. 1994, *Opt. Comm.*, 109, 16
- Mishchenko, M.I., Travis, L.D., & Mackowski, D.W. 1996, *JQSRT*, 55, 535
- Overbeck, J.W. 1965, *ApJ*, 141, 864

- Predehl, P., & Schmitt, J.H.M.M. 1995, *A&A*, 293, 889
- Purcell, E.M. 1979, *ApJ*, 231, 404
- Serkowski, K. 1973, in *Interstellar Dust and Related Topics*. IAU Symposium 52. Ed. J.M. Greenberg and H.C. van de Hulst. (Dordrecht: Reidel) p. 145
- Serkowski, K., Mathewson, D.L., & Ford, V.L. 1975, *ApJ*, 196, 261
- Slysh, V.I. 1969, *Nature*, 224, 159
- Smith, R.K., Edgar, R.J., & Shafer, R.A. 2002, *ApJ*, 581, 562
- Sofia, U.J., & Meyer, D.M. 2001, *ApJ*, 554, L221
- Temperton, C.J. 1983, *J. Comp. Phys*, 52, 1
- Temperton, C. 1992, *J. Scientific and Statistical Computing*, 13, 676
- van de Hulst, H.C. 1957, *Light Scattering by Small Particles*, (New York: Wiley)
- Vanlandingham, K.M., Schwartz, G.J., Shore, S.N. Starrfield, S., & Wagner, R.M. 2005, *ApJ*, 624, 914
- Waterman, P.C. 1971, *Phys. Rev. D* 3, 825
- Weingartner, J.C., & Draine, B.T. 2001, *ApJ*, 548, 296 (WD01)
- Whittet, D.C.B., Martin, P.G., Hough, J.H., Rouse, M.F., Bailey, J.A., & Axon, D.J. 1992, *ApJ*, 386, 562
- Wielgaard, D.J., Mishchenko, M.I., Marke, A., & Carlson, B.E. 1997, *Appl. Opt.*, 36, 4305
- Wiscombe, W.J. 1980, *Appl. Opt.*, 19, 1505
- Wiscombe, W.J. 1996, NCAR Technical Note NCAR/TN-140+STR, ftp://climate.gsfc.nasa.gov/pub/wiscombe/Single-Scatt/Homogen_Sphere/Exact_Mie/NCARMieReport.pdf
- Woo, J.W., Clark, G.C., Day, C.S.R., Nagase, F., & Takeshima, T. 1994, *ApJ*, 436, L5
- Yao, Y., Zhang, S.N., Zhang, X.L., & Feng, Y.X. 2003, *ApJ*, 594, L43
- Zubko, V., Dwek, E., & Arendt, R.G. 2004, *ApJS*, 152, 211

A. Least-squares fitting procedure

Let $n_c(a)$ be the number density of grains with composition c and radii $\leq a$. It is convenient to define $u \equiv \ln a$ and y_c such that $dn_c/d \ln a = dn_c/du \equiv \exp(y_c)$. Then dn_c/da is positive definite for $-\infty < y_c < \infty$.

The size distribution is sampled at N_{rad} sizes, and extinction and polarization are calculated at N_λ wavelengths.

The terms Ψ_j include the following contributions

$$\Psi_1 = \alpha_1 \left[\frac{V_{\text{sil}}}{V_{\text{sil},0}} - 1 \right] \quad (\text{A1})$$

$$\Psi_2 = \alpha_2 \left[\frac{V_{\text{car}} - V_{\text{PAH}}}{V_{\text{car},0}} - 1 \right] \quad (\text{A2})$$

$$\Psi_{2+j} = \frac{\alpha_3}{N_\lambda^{1/2}} \left[\frac{A_{\text{mod}}(\lambda_j)}{A_{\text{obs}}(\lambda_j)} - 1 \right] \quad j = 1, \dots, N_\lambda \quad (\text{A3})$$

$$\Psi_{N_\lambda+2+j} = \frac{\alpha_4}{N_\lambda^{1/2}} \left[\frac{p_{\text{mod}}(\lambda_j)}{p_{\text{obs}}(\lambda_j)} - 1 \right] \quad j = 1, \dots, N_\lambda \quad (\text{A4})$$

$$\Psi_{2N_\lambda+2+j} = \frac{\alpha_5}{(N_{\text{rad}} - 1)^{1/2}} \left[\min \left(\left(\frac{d \ln f}{du} \right)_{j+1/2}, 0 \right) \right]^2 \quad j = 1, \dots, N_{\text{rad}} - 1 \quad (\text{A5})$$

$$\Psi_{2N_\lambda+N_{\text{rad}}+2} = \alpha_6 [\max(f(a_{N_{\text{rad}}}) - 1, 0)]^2 \quad (\text{A6})$$

$$\Psi_{2N_\lambda+N_{\text{rad}}+1+j} = \frac{\alpha_7}{(N_{\text{rad}} - 2)^{1/2}} \left[\frac{d^2 y_{\text{sil}}}{du^2} \right] \quad a = a_j \quad j = 2, \dots, N_{\text{rad}} - 1 \quad (\text{A7})$$

$$\Psi_{2N_\lambda+2N_{\text{rad}}-1+j} = \frac{\alpha_8}{(N_{\text{rad}} - 2)^{1/2}} \left[\frac{d^2 y_{\text{car}}}{du^2} \right] \quad a = a_j \quad j = 2, \dots, N_{\text{rad}} - 1 \quad (\text{A8})$$

$$\Psi_{2N_\lambda+3N_{\text{rad}}-3+j} = \frac{\alpha_9}{(N_{\text{rad}} - 2)^{1/2}} \left[\frac{d^2 \ln f}{du^2} \right] \quad a = a_j \quad j = 2, \dots, N_{\text{rad}} - 1 \quad (\text{A9})$$

The radii a_j are assumed to be uniformly distributed in $u = \ln a$: $u_{j+1} - u_j = \Delta u$. The derivatives are evaluated using the usual differencing: $(df/du)_{j+1/2} = (f_{j+1} - f_j)/\Delta u$ and $(d^2 f/du^2)_j = (f_{j+1} + f_{j-1} - 2f_j)/(\Delta u)^2$.

Here $V_{\text{sil},0} = 2.29 \times 10^{-27} \text{ cm}^3/\text{H}$ and $V_{\text{car},0} = 1.57 \times 10^{-27} \text{ cm}^3/\text{H}$ are target values based on the estimated elemental abundances of species such as Mg, Si, Fe, and C, the fractions of these elements believed to be in solid form, and assumed densities for the silicate and carbonaceous material. For the target volume for silicate grains we assume a composition $\text{Mg}_{1.1}\text{Fe}_{0.9}\text{SiO}_4$, with $\text{Mg}/\text{H} = 3.3 \times 10^{-5}$, and density $\rho = 3.7 \text{ g cm}^{-3}$. This would consume 87%, 93%, 94%, and 29% of the current estimated solar composition values for Mg, Fe, Si, and O, respectively [$(\text{Mg}/\text{H})_\odot = 3.8 \times 10^{-5}$ (Grevesse & Sauval 1998), $(\text{Fe}/\text{H})_\odot = 2.9 \times 10^{-5}$ (Asplund et al. 2000), $(\text{Si}/\text{H})_\odot = 3.2 \times 10^{-5}$ (Asplund 2000), and $(\text{O}/\text{H})_\odot = 4.6 \times 10^{-4}$ (Asplund et al. 2004)]. For the target volume of

carbonaceous grains we assume 70% of the current estimated solar abundance $(\text{C}/\text{H})_{\odot} = 2.46 \times 10^{-4}$ (Asplund et al. 2005) to be in grains with $\rho = 2.2 \text{ g cm}^{-3}$.

The coefficients α_1 and α_2 weight the penalties for deviating from the target abundances; α_3 and α_4 weight the penalties for fractional errors in reproducing the observed extinction and polarization; α_5 weights the penalty if the alignment fraction $f(a)$ is not a monotonically-increasing function of size a ; α_6 and α_7 penalize non-smoothness in the size distributions; and α_8 penalizes non-smoothness in the alignment function.